# Energy transformation on flow-induced motions of multiple cylindrical structures with various corner shapes

Yibo Liang (梁艺博)[1], Longbin Tao[1, *], Longfei Xiao (肖龙飞)[2, 3]

[1] *Department of Naval Architecture, Ocean and Marine Engineering, University of Strathclyde, Glasgow, G4 0LZ, UK*

[2] *State Key Laboratory of Ocean Engineering, Shanghai Jiao Tong University, Shanghai, 200240, China*

[3] *Collaborative Innovation Centre for Advanced Ship and Deep-Sea Exploration, Shanghai, 20040, China*

## Abstract

A comprehensive numerical study on flow-induced motions (FIM) of a deep-draft semi-submersible (DDS), a typical multiple cylindrical structure in offshore engineering was carried out to investigate the energy transformation of the vortex shedding process. In addition, the corner shape effect on the flow characteristics, the hydrodynamic forces and the FIM responses are presented for a multiple cylindrical structure with various corner shapes (sharp, rounded and chamfered) under 45° current incidence. Different energy transformations, hydrodynamic characteristics and FIM responses were observed due to the slight variation of the corner shape. The galloping at 45° incidence for a square-section shape column was observed when the corner shape modified as a chamfered corner. A “re-attached vortex shedding” phenomenon is

* Corresponding author. Tel: +44 (0)141 548 3315
*Email address*: longbin.tao@strath.ac.uk

discovered when the "lock-in" happened for a chamfered corner design. Further insights of the fluid physics on the flow characteristics due to the difference of the corner shape are revealed. In addition, the energy transformation and the mechanism for reducing the hydrodynamic forces and the FIM responses are analysed.

## Keywords

Flow-induced motions (FIM); Vortex-induced motions (VIM); Corner shapes; Vortex shedding; Energy transformation; Galloping

## Introduction

Flow-induced motions (FIM) introduced a class of flows exhibiting a coupled interaction between fluid and structure. For example, vortex-induced motions (VIM) and galloping are some of this type of phenomenon. FIM attracts strong research interest in the field of fluid and structure interaction. Both VIM and galloping have received considerable attention in the offshore engineering discipline. Hydrodynamic problems of FIM with bluff column are often encountered during the operations of offshore platforms. Since the Genesis Spar commissioned in 1997 [1, 2], vortex-induced motion (VIM) – a cyclic rigid body motion induced by vortex shedding has been regularly observed on large floating offshore structures [3, 4] (e.g., Spar, semi-submersible and tension-leg platform) due to the long-term strong loop current in the Gulf of Mexico (GoM). Fujarra, *et al.*[2] well documented the literature about VIM during the last decade. When a current flow past an offshore platform, the vortices in the wake region can generate strong cyclic dynamic effects on the platform which is known as VIM. The VIM is mainly characterized as the motion in the horizontal plane leading to potential damage particularly causing the fatigue to mooring and riser systems. Apart from VIM, the FIM phenomenon of galloping is worth to investigate as well. Studies focusing on a typical square section cylinder with a flat face normal to the flow have been carried out in the aerodynamic discipline since Den Hartog[5] first proposed a criterion for the onset of galloping. However, there is still lack of understanding on the galloping in the hydrodynamic side.

Most of the floating platforms consist serval columns to support the superstructure. For a multi-column offshore platform (e.g. semi-submersible, tension-leg platform), vortex shedding occurs around each column. A strong vortex shedding interaction can be observed between each single column. Investigations on these interactions have been carried out by many researchers. Liu and Jaiman[6] performed a numerical study of vortex-induced vibrations (VIV) in a side-by-side cylinder arrangement. Li, et al.[7] further investigated the coupled dynamics of VIV adjacent to a stationary wall. Recently, a stability analysis of the flow-induced vibrations (FIV) of two cylinders in tandem arrangement was provided by Yao and Jaiman[8]. Even with considerable research effort on FIV, most of the current studies are still focusing on the low Reynolds number (Re ≈ 100) problem. Literatures on the FIV study at low Reynolds numbers have been published by different researchers focusing in various areas (e.g. Shen and Sun[9], Zhu, et al.[10], Jiao and Wu[11]), and most of them are expected to reveal more insight on the physics under high Reynolds number in future. To date, most of the study are still limited in the laminar flow problem. One of the contribution of the present work is that the Reynolds number in the current study reaches to the order of $10^4$, where turbulence plays an important role in the fluid-structure interaction during FIV.

In addition, cylinders investigated in the previous studies are either with a 2D assumption or are of an infinite length. It is noted that most of the floating structures in the ocean are with finite length columns and some of them are connected by pontoons. Therefore, the free end effect need to be examined. Rastan, et al.[12] recently performed a study on the flow around a single wall-mounted square cylinder at low Reynolds numbers. There are few papers contributing to the examination of the physics of FIV on a multi finite length column structure. Therefore, the second contribution of the present study is to provide a comprehensive numerical study to examine the mechanism of FIV on a multi finite length column structure based on our well-validated numerical model [13, 14].

Apart from the Reynolds number and the free end effect, the shape of the column, especially the corner shape, affects the hydrodynamic and FIM responses. The corner shape of the column can alter the vortex shedding characteristics around columns significantly. Bearman, *et al.*[15] experimentally investigated the corner radius influence on the force experienced by a square or diamond section-shaped column in an oscillating flow. Their study showed that the drag coefficient of a diamond section decreases with increasing the corner radius. However, the square section does not show a clear relationship between drag coefficient and corner radius. Subsequently, Hu, *et al.*[16] experimentally studied the corner radius effects on a square prism based on the particle image velocimetry (PIV) measurement in the wake region. Liu, *et al.*[17] recently carried out a numerical study about the corner radius effects on VIM of a semi-submersible, and reported that the transverse motion is significantly affected by the corner ratio of the column. Tamura, *et al.*[18] performed a numerical study on flow over a square column with different corner shapes including sharp, rounded and chamfered. Both hydrodynamic force and pressure distribution were discussed in their study. Subsequently, Tamura and

Miyagi[19] implemented a wind tunnel test to obtain the static hydrodynamic forces (drag and lift forces) on the cylinder with various corner shapes, and the authors confirmed that the chamfered and rounded corners lead to decreased drag forces, as a result of a reduction in wake width. Recently, Cao and Tamura[20] further performed a numerical study on supercritical flow past a square cylinder with rounded corners. However, the square cylinder itself is still a stationary structure without any motions coupled in the simulation. Despite the aforementioned efforts, there is still lack of comprehensive understanding of the corner shape effect, especially on the motions induced by the vortex shedding due to different corner shapes. The third contribution of the current work is to provide insights on the corner shape effect.

It is also worth noting that most research on a square cylinder focused on an angle of attack at 0 degree where FIM is dominated by galloping. At an angle of attack at 45 degree, however, VIM dominates FIM. Zhao, et al.[21] defined the branch/mode competition in the flow-induced motions of a single square cylinder. The energy transformation between the fluid and the single cylinder are well examined in their experimental tests. Unlike most of the previous studies on FIM, the time-frequency domain is analysed by using continuous wavelet transforms (CWT) instead of Fast Fourier Transform (FFT). As a traditional way, FFT has been used by many researchers on studies of FIM, Zhao, et al.[22] well-illustrated the flow pattern against oscillating amplitude, frequency and phase characteristics. Liu, et al.[17] also tried to used frequency domain analysis to investigate FIM. Gonçalves, et al.[23] applied Hilbert-Huang Transform (HHT) to examine the frequency characteristics of FIM. It is noted that Continuous Wavelet Transform (CWT) is very efficient in determining the damping ratio of oscillating signals (e.g. identification of damping in dynamical systems). CWT can illustrate the time history in the frequency domain. This new routine can provide more information on the energy transformation between the fluid and oscillating structure leading to a better understanding of FIM. Apart from analysing the energy transformation on the frequency domain, the work done is a straight way to observe the energy transformation process. Antony, et al.[24] investigated the work done by each column of a multi-column floating structure through experiments. Liang and Tao[25] later performed a numerical study on the work done by each column on a multiple cylindrical structure. Apart from analysing the energy transformation in frequency domain, calculating the work done by the structure is a straightforward way to observe the energy transformation process. Antony, et al.[24] investigated the work done by each column of a multi-column floating structure through experiments. Liang and Tao[13] later performed a numerical study on the work done by each column on a multiple cylindrical structure.

Based on the literature, a comprehensive numerical investigation is performed in the present study to reveal further insights of the fluid physics on the effects of corner shape design on vortex shedding characteristics and associated VIM by examining the energy transformation of the hydrodynamic phenomenon. Considerable studies are provided in the present work to exam the energy transformation based on the continuous wavelet transform (CWT). It is confirmed that the flow characteristics, hydrodynamic forces and the related VIM responses altered dramatically by varying the corner shape. Additionally, the galloping at 45° incidence for a square-section shape column was observed when the corner shape modified as a chamfered corner.

# 1. Fundamental description of FIM phenomenon

## 2.1. Description of FIM

As a typical cyclic rigid body motion, FIM is induced by vortex shedding from a large-sized floating structure. When the current flow over a floating cylindrical structure, the dynamics of the structure will be affected by the vortices that are generated and then systematically shed in the downstream region, may begin oscillating either in a side to side or in a fore and aft manner. If the vortex shedding frequency is approaching to the natural frequency of the structure, a so-called "lock-in" phenomenon can occur, which could amplify the cyclic motions of the structure dramatically. This resonance phenomenon may lead to potential damage to offshore systems, especially causing fatigue of the mooring and riser systems.

## 2.2. Key parameters for FIM

To better understand the phenomenon of FIM, primary non-dimensional parameters have been introduced into the present work. In this section, all the key non-dimensional parameters are presented following the equations to give general information describing FIM.

The so-called reduced velocity (*Ur*) is normally used as the reference value when discussing FIM, and is defined as:

$$Ur = \frac{UT_n}{D} \tag{1}$$

where $U$ is the current speed, $T_n$ is the natural period of the structure motions in calm water and $D$ is the projected length of the column.

The resonance "lock-in" phenomenon for FIM problems always occurs at $Ur \approx 7$ indicating the natural frequency of the motion, $f_n$, is close to the vortex shedding frequency, $f_v$. A dimensionless variable named as Strouhal number ($St$) is often used to represent the vortex shedding frequency, which is given by:

$$St = \frac{f_v D}{U} \qquad (2)$$

where $f_v$ is the vortex shedding frequency that is obtained from the power spectra of the lift force fluctuations as suggested by Schewe[26], $U$ is the free stream velocity and $D$ is the projected width of the column. The Strouhal number for square cylinders, depending on the current incidence, were shown to be 0.13 and 0.17 for 0° and 45° incidence respectively. These results were obtained by Norberg[27] from his experimental study.

As the vortex shedding is a flow separation phenomenon, the Reynolds number is used to describe the level of the flow separation.

$$Re = \frac{UD}{v}, \qquad (3)$$

where $U$ is the free stream velocity, $D$ is the projected width of the column and $v$ is the kinematic viscosity of the fresh water.

With Reynolds number increases, the flow characteristics around a cylinder will have different separation phenomena due to the viscous effects. The vortex shedding phenomenon can vary significantly by increasing the Reynolds number.

When flow over a cylindrical structure, the vortices periodically shed from each side of the cylinder can generate cyclic hydrodynamic loads onto the structure. The hydrodynamic loads are presented as the drag force coefficient ($C_D$) and the lift force coefficient ($C_L$), which are defined as:

$$C_D(t) = \frac{F_D(t)}{\frac{1}{2}\rho U^2 A_{projected}}, \qquad (4)$$

$$C_L(t) = \frac{F_L(t)}{\frac{1}{2}\rho U^2 A_{projected}}, \quad (5)$$

where, $F_D(t)$ is the drag force on the structure, $F_L(t)$ is the lift force on the structure, $\rho$ is the density of the fresh water, $U$ is the free stream velocity and $A_{projected}$ is the projected area.

By excluding the wave impact, the hydrodynamic forces $F_D(t)$ and $F_L(t)$ due to current on the structure are calculated by the equation[28]:

$$m\ddot{X}(t) + C\dot{X}(t) + K_x X(t) = F_x(t) \quad (6)$$

$$m\ddot{Y}(t) + C\dot{Y}(t) + K_y X(t) = F_y(t) \quad (7)$$

where $m$ is the platform mass; $C$ is the structural damping coefficient; $K_x$ and $K_y$ are the linear spring constant in the in-line and transverse directions; $X(t)$ and $Y(t)$ are the displacement at in-line and transverse direction, respectively; $F_x(t)$ and $F_y(t)$ represent the in-line and transverse hydrodynamic forces acting on the structures.

The structural damping coefficient is very small and can be disregarded. The hydrodynamic forces which include added mass and hydrodynamic damping forces due to fluid are placed on the right side of the equations.

To characterize the level of FIM in general, the non-dimensional characteristic amplitude ($A/D$) is chosen as the common variable[2, 3, 23, 29], which is defined as:

$$A/D = \sqrt{2} \times \sigma\left(\frac{y(t)}{D}\right), \quad (8)$$

where $\sigma$ is the standard deviation of the time series $y(t)/D$, and $y(t)$ represents the time series of in-line, transverse and yaw motions. For the rotational yaw motion, the non-dimensional amplitude is defined as $\sqrt{2}\times\sigma(yaw(t))$.

## 2. Numerical simulation

In the present study, the deep-draft semi-submersible consists of 4 columns. The vortices shed from each column will generate periodically hydrodynamic loads on the overall structure. Thus, the shapes of the columns and the subsequent interactions between the individual vortex shedding processes due to each column, characterize the VIM responses.

**Fig. 1** shows an overview of the semi-submersible along with the chronological order of the columns. In **Table 1**, the model characteristics of the semi-submersible were illustrated. As shown in **Fig. 2**, four horizontal mooring lines are attached to restrain the horizontal motions of the semi-submersible model. In the present numerical model, the horizontal stiffness at both the transverse and in-line directions is 66.5 N/m which was scaled from a prototype mooring design. In addition, only three degrees freedom motions in the horizontal plane (namely transverse, in-line and yaw) were allowed in the numerical simulations.

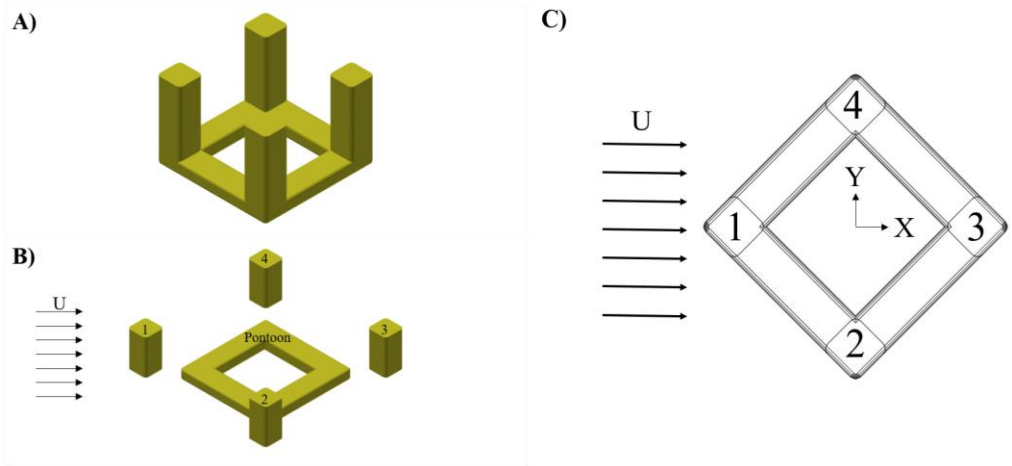


**Fig. 1** Numerical model (rounded corner as an example) simulated in the present study (A is the entire model; B is the decomposed model which shows the definition of the individual members; C is the sketch of the semi-submersible).

**Table 1** Principle dimensions of the model semi-submersible (with a scale ratio of 1:64).

| | **Model （m）** |
|---|---|
| **Distance between centre columns (*S*)** | 1.133 |
| **Column width (*L*)** | 0.305 |
| **Immersed column height above the pontoon (*H*)** | 0.578 |
| **Pontoon height (*P*)** | 0.156 |

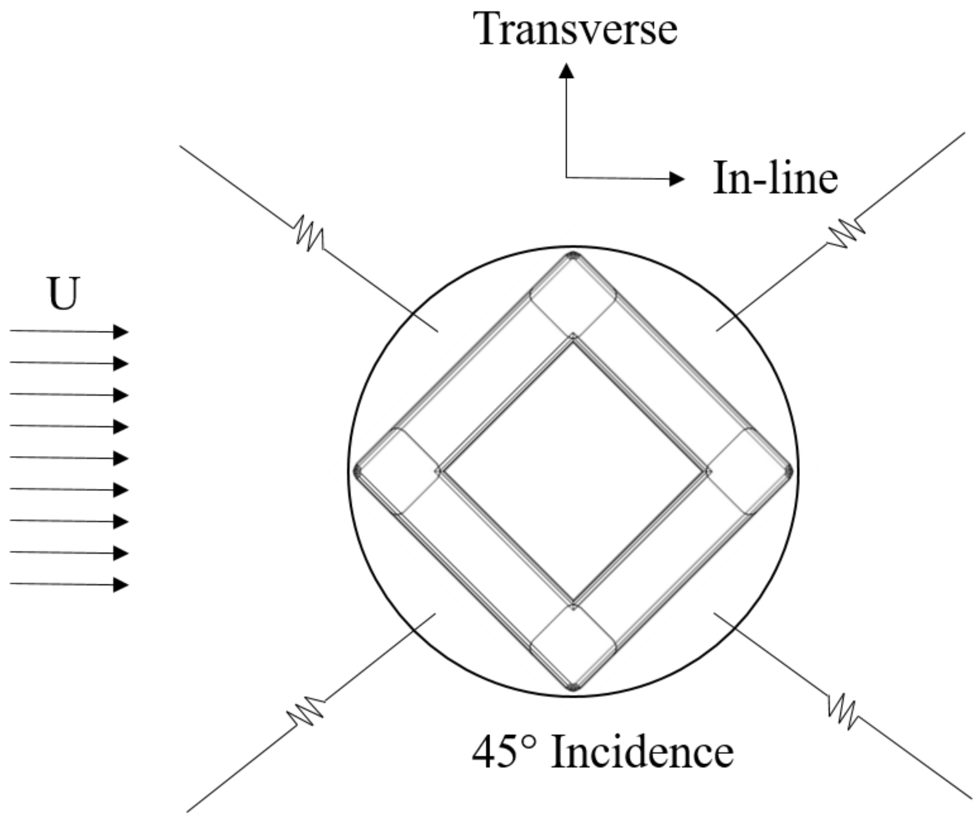


**Fig. 2** Schematic of the mooring set-up.

The semi-submersible models with different corner shapes of the column are shown in **Fig. 3**. The corner ratios for both rounded corner and chamfered corner are 15% of the column width which is well within a typical range (10% ~ 20%) for designing the column of offshore platforms. Considering the contribution to buoyancy and the convenience of construction, the design of pontoons, horizontal structural members is kept the same for all three corner shape design. The geometry characteristics of all semi-submersibles are the same except for the corner shape. It is noted that, due to the corners being modified, the projected widths of each column design are slightly different at 45 degree incidence (as shown in **Fig. 3**). Additionally, the mass ratio (ratio of mass to displacement) is exactly the same for all three models. The Reyonlds number is ranging from $3.6 \times 10^4$ to $1.1 \times 10^5$ in the present study.

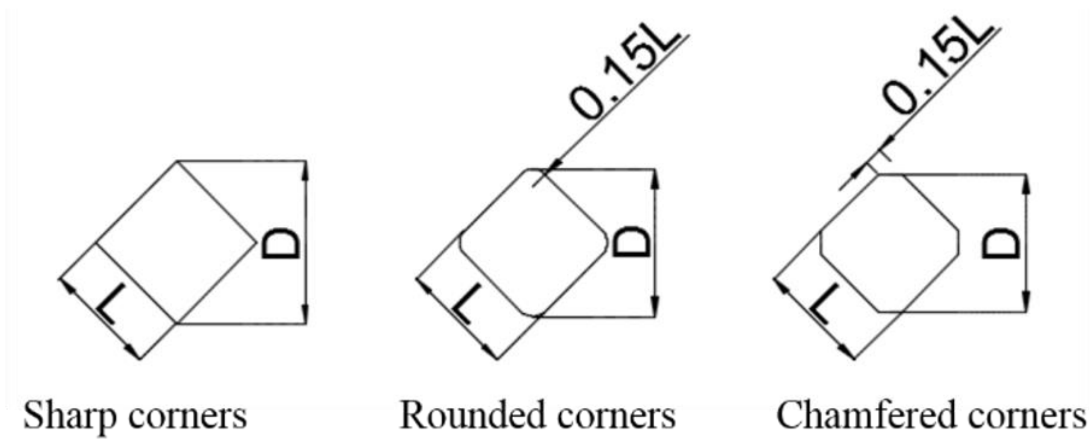


**Fig. 3** Column sectional configurations.

## 3.1. Numerical scheme

The improved delayed detach eddy simulation (IDDES) model [30] with the Spalart-Almaras (SA) [31] was used in this study. IDDES is a model capable of building a single set of formulas both for natural (D)DES applications and for the wall-modelling in large eddy simulation (WMLES) [30]. The delayed detach eddy simulation (DDES) length scale is implemented to eliminate the modelled-stress depletion in the original DES approach, while WMLES is applied to achieve more accurate prediction of the mean velocity in the boundary layer. The boundary layers and irrotational regions are solved using the SA model. However, when the grid is fine enough, it will emulate a basic large eddy simulation (LES) subgrid scale model in the detached flow regions [32]. It is noted that the SA model requires $y^+ < 1$ (where $y^+ = u_* \Delta y_1 / \nu$, and where $u_*$ denotes the friction velocity at the nearest wall, $\Delta y_1$ is the first layer thickness and $\nu$ is the kinematic viscosity) indicating that the viscous sublayer is properly resolved. All the simulations were carried out using a commercial CFD package, STAR-CCM+ 9. The finite volume method (FVM) is adopted to discretize the incompressible flow field[33]. The second-order implicit three time levels (ITTL) scheme is applied for the temporal discretization. The convective term is evaluated by using a hybrid second-order upwind scheme. The SIMPLE algorithm is employed to treat the pressure and velocity coupling.

The governing Navier-Stokes equations solved for the incompressible flow can be written as:

$$\nabla \cdot \bar{u} = 0, \tag{9}$$

$$\frac{\partial \bar{u}}{\partial \bar{t}} + \bar{u} \cdot \nabla \bar{u} = -\frac{1}{\rho} \nabla \bar{p} + \nu \nabla^2 \bar{u} + \frac{1}{\rho} \nabla \tau \tag{10}$$

where $\nabla$ is the Hamiltonian operator; $u$ is the velocity vector; $t$ is the time; $p$ is the pressure; $\rho$ is the density of water; $\upsilon$ is the kinematic viscosity of the water; The last term of Equitation (10) is the Reynolds stress tensor $\tau = -\rho(\overline{u'u'})$, where $u'$ denotes the fluctuating velocity. The Reynolds stress tensor is an additional term that represents the effects of turbulence.

## 3.2. Computational domain.

The computational domain size is chosen based on previous experience with modelling vortex-induced motions of the benchmark DDS over a similar parameter space [14]. For all of the simulations, a $9B_L \times 6B_L \times 3B_T$ sized computational domain (see **Fig. 4**) was used in the present simulations (where $B_L$ is the overall width of the structure and $B_T$ is the draft of the structure). More specifically, the domain was considered to be sufficiently large to eliminate both the far field effects from the boundaries and the three-dimensional effects from a spanwise cross flow direction [13, 14].

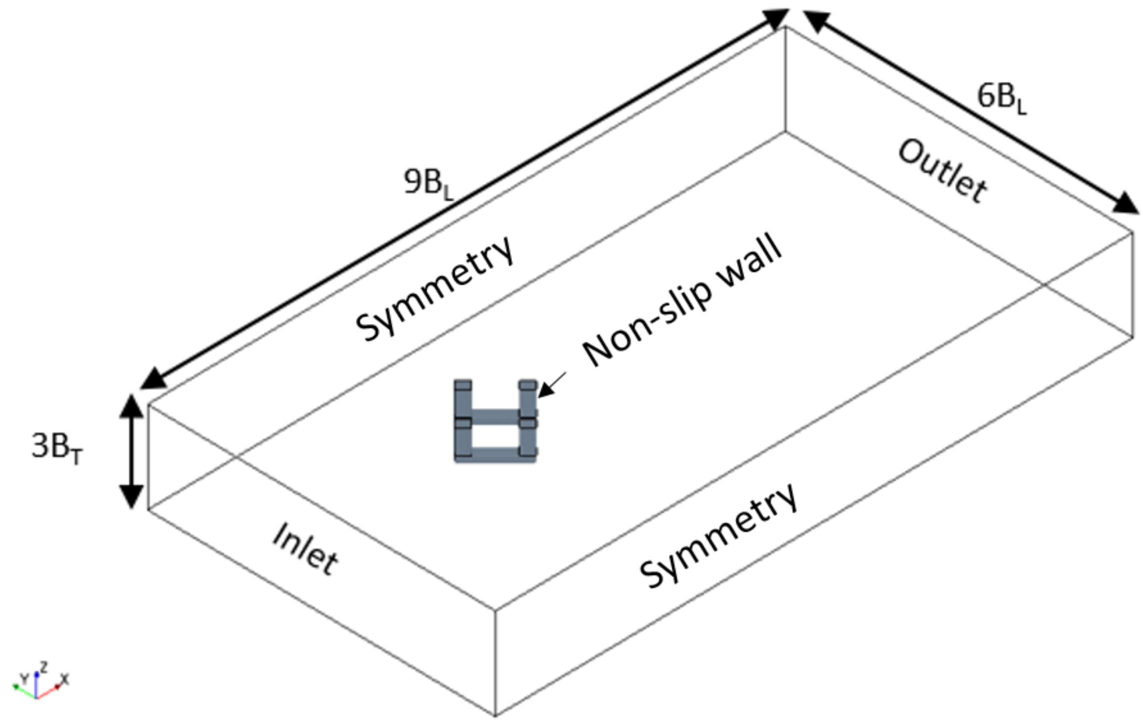


**Fig. 4** Computational domain.

The computational domain was modelled with a three-dimensional mesh of elements. A polyhedral mesh [32] was used in this study. The overall element mesh domain is illustrated in **Fig. 5**. In the present study, a near wall refinement method named "Prism Layer Mesher [32]" was adopted with a core volume mesh to generate orthogonal prismatic cells next to wall surfaces. This layer of cells is necessary to improve the accuracy of the flow solution [32]. The $y^+$ values were smaller than 1 in all simulations to improve the performance of the boundary layer simulation. Five regional refinements were added in the domain in order to refine both the near wake and the far wake regions.

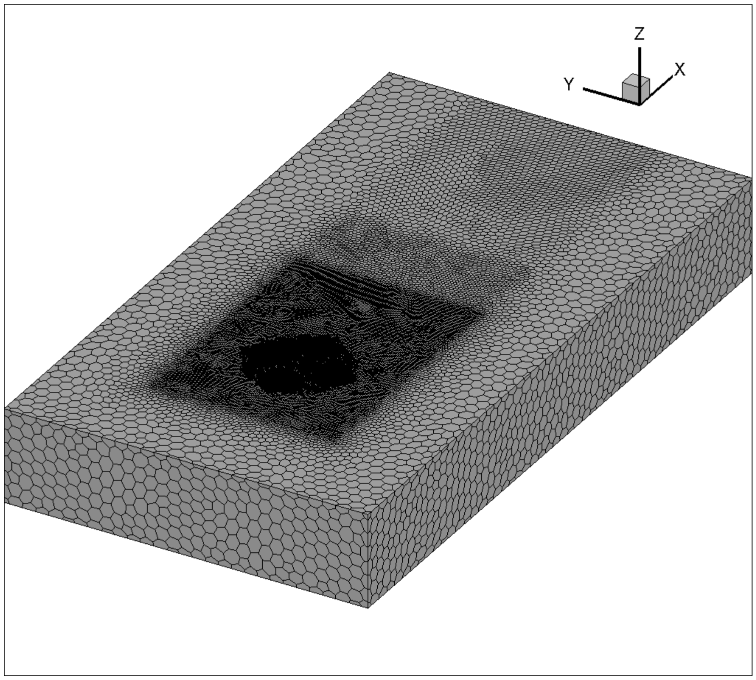


**Fig. 5** Visualization of the mesh of the semi-submersible.

The boundary conditions are kept the same in all the simulations. At the inlet, a uniform and constant flow velocity is specified directly for all sensitivity studies. Along the outlet boundary, the pressure is prescribed to be equal to zero. The velocity at the boundary is extrapolated from the interior using reconstruction gradients [32]. For the body surface of the semi-submersible, a no-slip boundary condition is specified[32]. It is noted that the Froude number is quite small ($Fr < 0.2$, $Fr = U/\sqrt{gD}$, where $U$ is the current velocity, $g$ is the acceleration of gravity and $D$ is the projected width of the column) in all simulations of the present investigation. As observed in the physical model tests [13], the free surface effects were rather limited and can be ignored. Therefore, only the submerged geometry is considered, and the geometry of the structure above the waterline will not affect the simulation results.

3.3. Sensitivity study and Validation

In order to investigate the numerical mesh sensitivity of the calculated results, a mesh sensitivity study had been carried out with different levels of refinement grids resolution following the guideline proposed by Celik, *et al.*[34] at a Reynolds number of $1.1 \times 10^5$. Mesh refinement are varied from coarse (with a grid number of $9.4 \times 10^5$) to fine (with a grid number of $6.9 \times 10^6$). Additionally, a time step convergence study had been performed with the non-dimensional time step ($\Delta tU/D$, where $\Delta$t is the time step, $U$ is the inlet velocity and $D$ is the projected length of the column) varied from 0.016 to 0.004. Comprehensive description with details of the procedure on the mesh and time step convergence study can be found in our previous works [13, 14] . In the present work, the non-dimensional time step is chosen as 0.008 with a grid number of $3.4 \times 10^6$ [13, 14]. Additional convergence test is conducted in the present investigation, namely the numerical model with a rounded corner is further validated with the experimental measurements obtained from the towing tank test [14]. In the present study, the results for all cases were obtained by averaging after more than fifteen FIM oscillation cycles.

**Table 2** Validation of the natural periods of the motions in calm water.

| | **Natural period of transverse motion,** $T_{0transverse}$ **(s)** | **Natural period of yaw motion,** $T_{0yaw}$ **(s)** |
|---|---|---|
| **Numerical** | 20.5 | 19.7 |
| **Experimental [14]** | 20.1 | 18.3 |

In **Table 2**, the natural period obtained from the present numerical model is validated against the experimental data. It is shown that the present numerical model has a good agreement with the experimental results (7.7% relative variation for yaw motion and 2.0% relative variation for transverse motion).

As can be seen in **Fig. 6**, the present numerical predictions show a good agreement with the previous experimental results for both hydrodynamic forces and motion response. Thus, the numerical model can be applied with confidence in future VIM simulations.

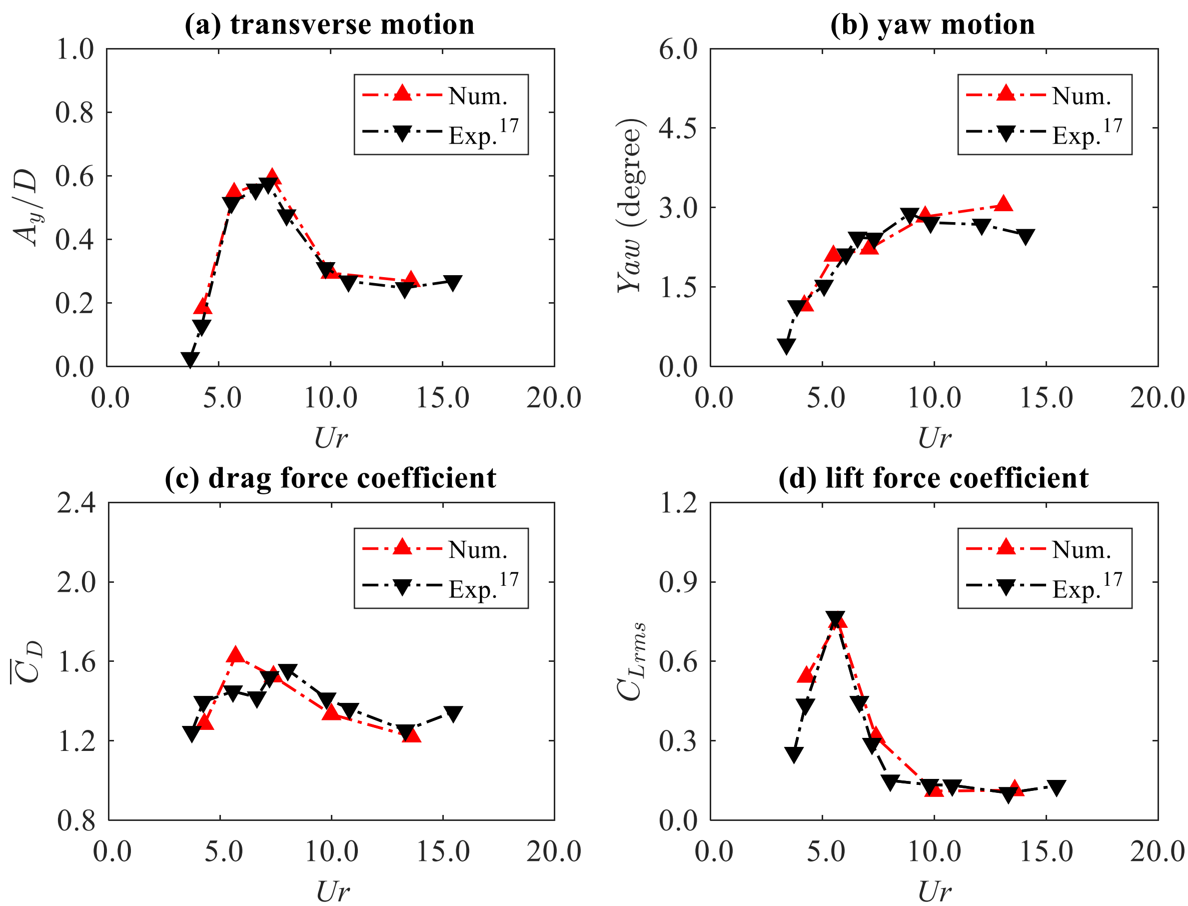


**Fig. 6** Validations between the present numerical model (rounded corner) and previous experimental results. (a) non-dimensional transverse amplitude; (b) non-dimensional yaw amplitude; (c) mean drag coefficient; (d) root-mean-square lift coefficient.

## 3. Results and discussion

Comprehensive numerical simulations of VIM were conducted to examine the effects of corner shape. The motion responses, hydrodynamic forces and flow patterns around DDS with columns of three different corner shapes are investigated under five reduced velocities with a current heading of 45 degree. All the results were collected for simulations more than fifteen cycles of the VIM transverse oscillation period in the present study.

### 4.1. Natural period of the motions in calm water

**Table 3** illustrates the numerical predictions of the natural period of the motions in calm water. It demonstrates that the rounded corner shape structure has the smallest natural period among the three designs while the DDS with sharp corner design has the largest natural period. This is mainly due to the modification of the corner decreasing the hydrodynamic damping of the structure.

**Table 3** Natural periods of the motions in calm water.

| **Corner shape** | **Natural period of transverse motion,** $T_{0transverse}$ **(s)** | **Natural period of yaw motion,** $T_{0yaw}$ **(s)** |
|---|---|---|
| **Sharp** | 21.3 | 20.3 |
| **Rounded** | 20.5 | 19.7 |
| **Chamfered** | 20.6 | 19.7 |

### 4.2. Energy transformation on flow-induced motions

During the FIM process, the energy can be transferred between the fluid flow and the oscillating structure. Motion response and hydrodynamic forces are generated as a result of the energy transformation. In order to gain some deep insights of the transformation process, frequency domain analysis is provided in the present study. The phase angle between the lift coefficient and transverse motion amplitude are further discussed. As a straightforward way to observe the complex energy transformation, the work done on different structure members are further calculated and presented.

#### 4.2.1. Motion characteristics

**Fig. 7**, which compares the numerical results among three different corner shape designs, presents the non-dimensional characteristic amplitudes (transverse, in-line and yaw motions) under 45 degree incidence. As seen in **Fig. 7**, the largest $A_y/D$ for all three design occurs at $Ur \approx 7.0$. The "lock-in" region occurs in the range of $6.0 \leq Ur \leq 9.0$. The structure with rounded corner shows the most significant motion in the transverse motion. It can be observed that the structure with the sharp corner design has the best transverse motion response among the structures with three different corner shapes. However, as shown in **Fig. 7**, the non-dimensional transverse amplitudes of the structure with chamfered corner are very close to the rounded corner cases in the "pre lock-in" and "lock-in" regions. Since the project length of the chamfered corner column is 93% of the rounded corner column's project length, the actual transverse motion response of the structure with chamfered corner is smaller than the rounded corner case in the "pre lock-in" and "lock-in" regions. It is noticed that the chamfered corner case has a rapid increment in the "post lock-in" region for all three horizontal mode motions. In contrast to the sharp and rounded corners, the galloping at 45° incidence for a square-section shape column was clearly evident when the corner shape modified as chamfered where the motion response increases without self-limiting (see **Fig. 7**). Regarding the in-line motion, the "lock-in" occurs for a sharp corner structure is found at $Ur \approx 9$. By modifying the corner shape, the "lock-in" is shifted to a smaller $Ur$. The "lock-in" in the in-line direction occurs for a rounded corner structure is around $Ur = 7$, while for a chamfered corner structure, the "lock-in" occurs at $Ur \approx 6$. It is observed that the rounded corner and chamfered corner cases have similar yaw motion responses, and the structure with sharp corner significantly reduced the yaw motion responses.

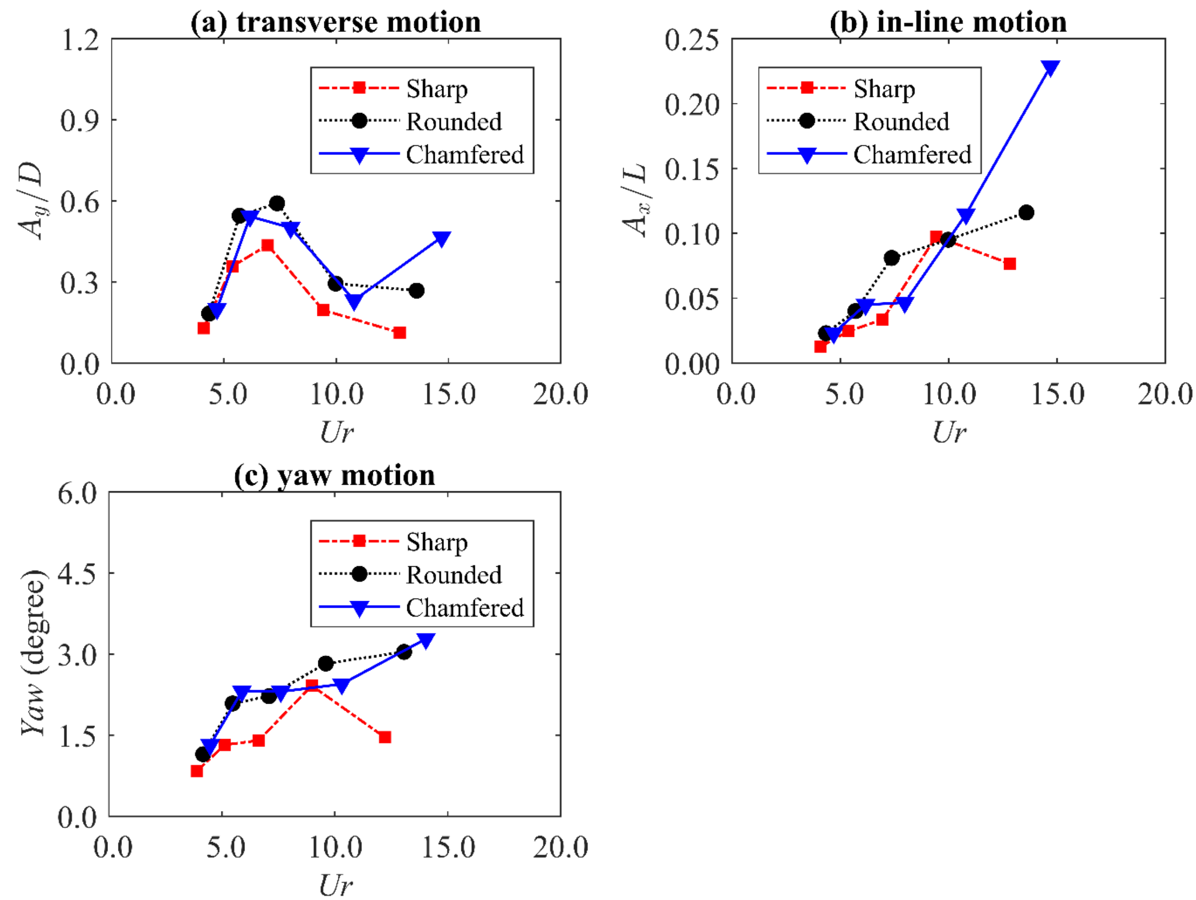


**Fig. 7** Non-dimensional transverse, in-line and yaw characteristics amplitudes. (a) Transverse motion; (b) in-line motion; (c) yaw motion.

4.2.2. Drag and lift forces on the structure

In addition to the motion responses, the drag and lift coefficient for all three designs are evaluated and shown in **Fig. 8**. It is clearly observed that, the chamfered corner has the largest $\overline{C}_D$ among three corner shape designs. This is due to the chamfered corner has introduced a flat plane into the projected area normal to the current direction. The flat plane at the chamfered corner can increase the drag force on the column. For the lift coefficient, it is shown that the sharp corner case has the minimum $C_{Lrms}$ which leads the structure exhibiting the smallest transverse motion among all three corner shape designs. It is noted that the near-wake flow structure is sensitive to the change of the leading corner design. For a sharp corner column, the flow separation point is fixed on the leading corner edge. However, for a rounded or chamfered corner design, the separation point changes during the motion. As the pressure distribution is altered due to the reattachment on the lateral face strongly influencing the pressure distribution on the column, the fluctuation lift force on the column is changed accordingly. Therefore, it further leads to a structure with a sharp corner showing $C_{Lrms}$ being significantly reduced. As shown in **Fig. 8**, both $\overline{C}_D$ and $C_{Lrms}$ increase when "lock-in" occurs as the consequence of the fluctuations of the force on the structure excited by resonance.

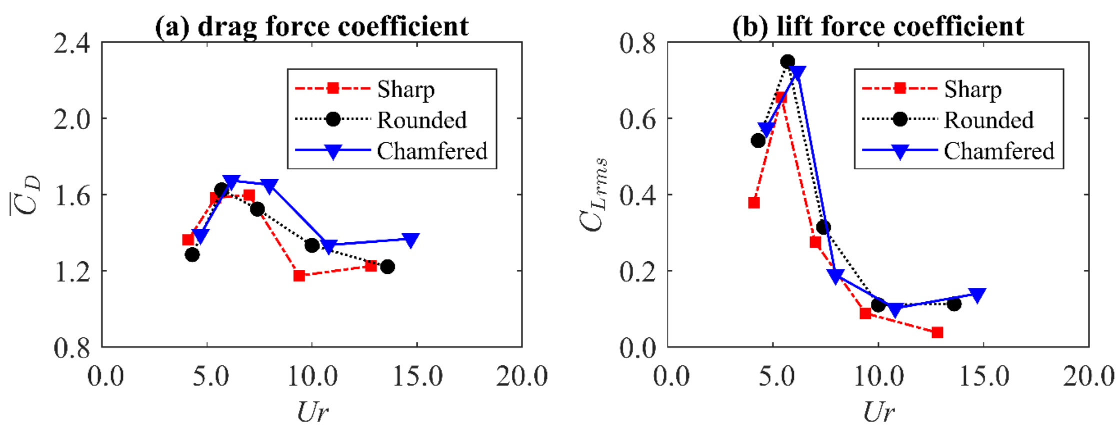


**Fig. 8** Mean drag coefficient ($\overline{C}_D$) and root mean square lift coefficient ($C_{Lrms}$). (a) mean drag force coefficient; (b) root mean square lift coefficient.

4.2.3 Motion trajectory and lift coefficient time history.

**Fig. 9**, **Fig. 10** and **Fig. 11** present the time history of transverse motion and lift coefficient for three different corner designs respectively. Also shown in the figures are the Power Spectrum Density (PSD) for both transverse motion and lift coefficient obtained by transferring to the frequency domain. The fluctuation of lift coefficients for all three designs are synchronised (have the same phase angle and fluctuation period) with the transverse motions in the “pre lock-in” and “post lock-in”. Especially for the sharp corner design, the transverse motion and lift coefficient are fully synchronised when *Ur* = 7 where the “lock-in” occurs. This indicates that the energy dissipated by the damping is closed to the energy added by the external force. The system therefore reaches its maximum amplitude. However, in the present study, when the motions of the structure shift to the “post lock-in” region, the fluctuation of lift coefficients for all three corner designs are no longer synchronised with the transverse motions. As seen in **Fig. 9** (g) (i), **Fig. 10** (g) (i) and **Fig. 11** (g), a phase delay has been observed in the “post lock-in” region. To further elucidate the response of the structure and the lift force on the structure for various reduced velocities, the power spectrum density of the transverse motions and the lift coefficient are present in **Fig. 9**, **Fig. 10** and **Fig. 11**. The dominant transverse motion frequency and vortex shedding frequency are both close to the transverse natural frequency in still water at the “pre lock-in” and “lock-in” regions ($f_y/f_N$ and $f_s/f_N \approx 1$). In addition, a new phenomenon is observed for the chamfered design at *Ur* = 6.2. Unlike the sharp or rounded corner, in the “lock-in” region, a relatively small peak (0.1% amplitude of the dominated peak) is observed in the frequency domain (see **Fig. 11** (d)) apart from the dominated peak (especially for the $C_L$). This indicates that there is a “secondary vortex-shedding” phenomenon existing during the “lock-in”. Further discussion based on the flow patterns will be provided in section 4.3.

In addition to the motion response of and hydrodynamic forces on the structures, the frequency response, as well as the phase angle between the transverse motion and the lift coefficient of the structure, can provide further insight over the energy transfer from the fluid flow to the structure during VIM. Thus, the non-dimensional response frequency $f_y/f_N$ and non-dimensional vortex shedding frequency $f_s/f_N$ are presented in **Fig. 12**. It is noted that $f_y/f_N$ and $f_s/f_N$ are the same at the "pre lock-in" and "lock-in" region for all three different corner designs with a value of approximately 1. When the VIM shifted to the "post lock-in" region, the non-dimensional vortex shedding frequency is increased and the non-dimensional response frequency is equal to $f_s/f_N$ at $Ur \approx 10$. Beyong $Ur \approx 12$, however, $f_y/f_N$ is evidently bifurcating while $f_s/f_N$ continues to increase. Two equal weighted peaks (purple circles in the figures) are observed in **Fig. 9** (i), **Fig. 10**(i), and **Fig. 11**(i). It is noted that the dominant peak $f_y/f_N$ is decreased, gradually moving away from $f_s/f_N$ and dropping below the dividing line of $f/f_N = 1$. However, the significant secondary peak of $f_y/f_N$ (* marked in **Fig. 12**) still remains the same as $f_s/f_N$.

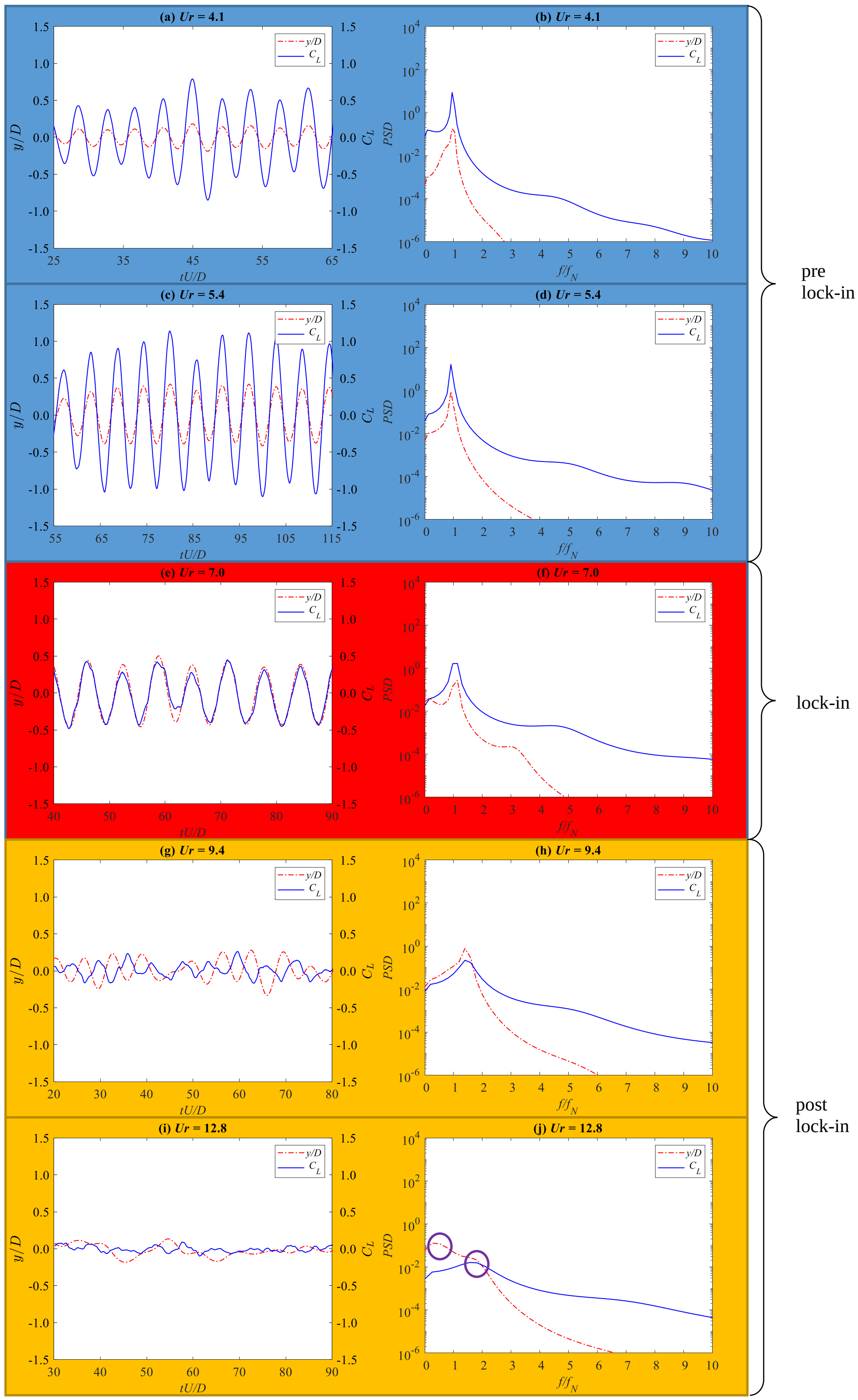


**Fig. 9** Time history of lift coefficient and transverse motion for sharp corner design. (a, c, e, g, i are in time domain; b, d, f, h, j are in the frequency domain). (a) Motion trajectory and lift coefficient time history at *Ur* = 4.1; (b) Motion trajectory and

lift coefficient in frequency domain at *Ur* = 4.1; (c) Motion trajectory and lift coefficient time history at *Ur* = 5.4; (d) Motion trajectory and lift coefficient in frequency domain at *Ur* = 5.4; (e) Motion trajectory and lift coefficient time history at *Ur* = 7.0; (f) Motion trajectory and lift coefficient in frequency domain at *Ur* = 7.0; (g) Motion trajectory and lift coefficient time history at *Ur* = 9.4; (h) Motion trajectory and lift coefficient in frequency domain at *Ur* = 9.4; (i) Motion trajectory and lift coefficient time history at *Ur* = 12.8; (j) Motion trajectory and lift coefficient in frequency domain at *Ur* = 12.8.

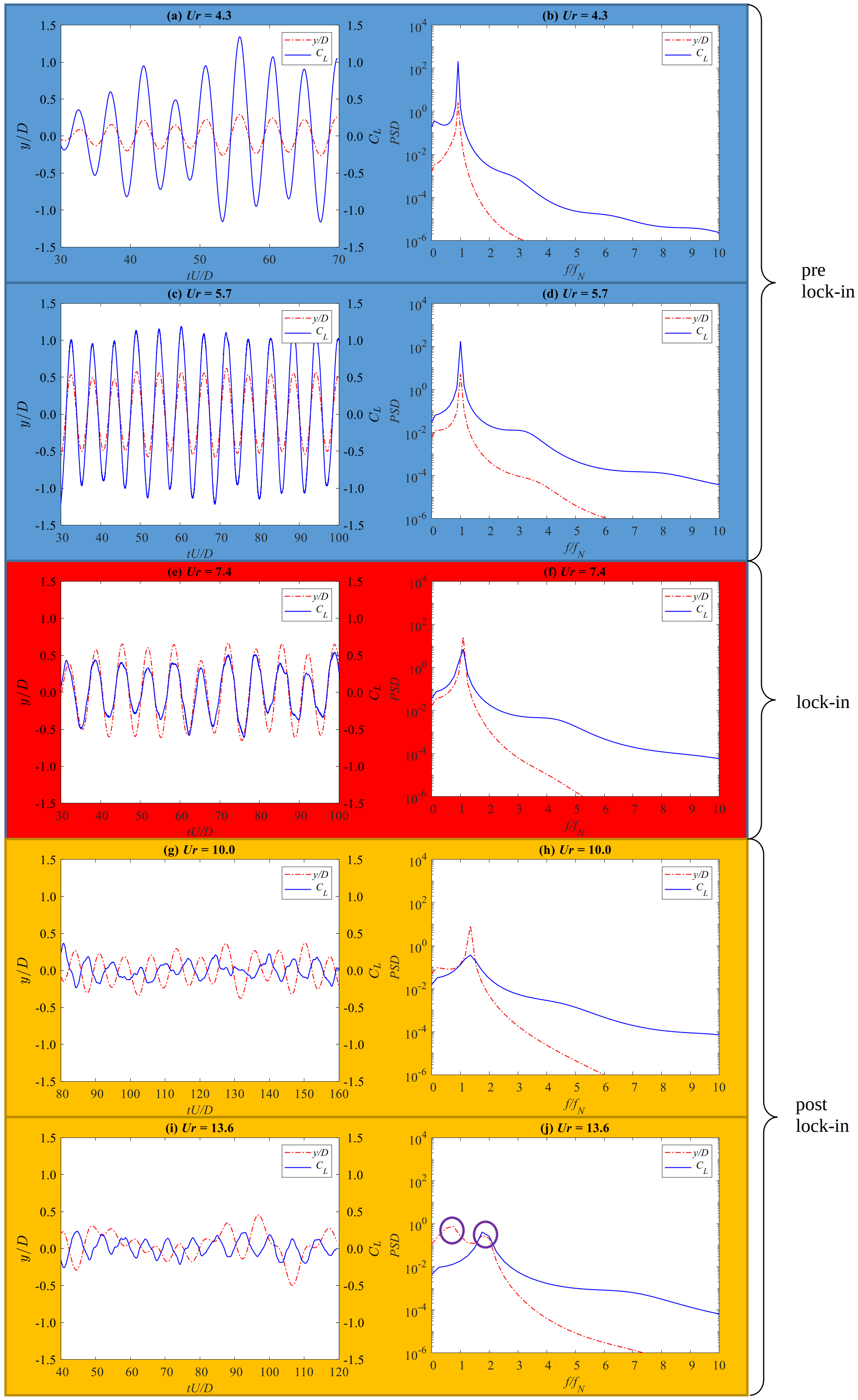


**Fig. 10** Time history of lift coefficient and transverse motion for rounded corner design. (a, c, e, g, i are in time domain; b, d, f, h, j are in the frequency domain). (a) Motion trajectory and lift coefficient time history at *Ur* = 4.3; (b) Motion trajectory and

lift coefficient in frequency domain at *Ur* = 4.3; (c) Motion trajectory and lift coefficient time history at *Ur* = 5.7; (d) Motion trajectory and lift coefficient in frequency domain at *Ur* = 5.7; (e) Motion trajectory and lift coefficient time history at *Ur* = 7.4; (f) Motion trajectory and lift coefficient in frequency domain at *Ur* = 7.4; (g) Motion trajectory and lift coefficient time history at *Ur* = 10.0; (h) Motion trajectory and lift coefficient in frequency domain at *Ur* = 10.0; (i) Motion trajectory and lift coefficient time history at *Ur* = 13.6; (j) Motion trajectory and lift coefficient in frequency domain at *Ur* = 13.6.

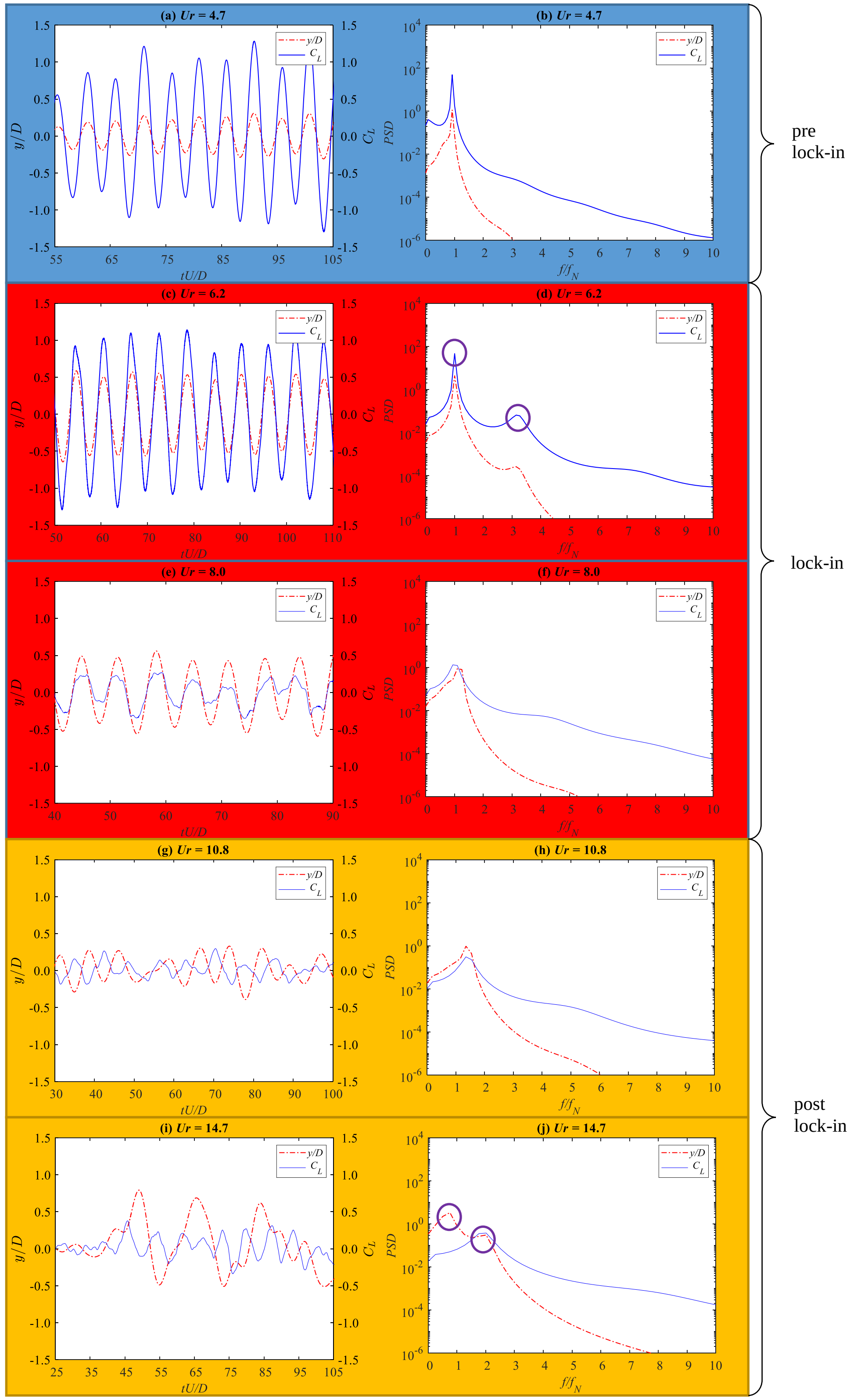


**Fig. 11** Time history of lift coefficient and transverse motion for chamfered corner design. (a, c, e, g, i are in time domain; b, d, f, h, j are in the frequency domain).

(a) Motion trajectory and lift coefficient time history at *Ur* = 4.7; (b) Motion trajectory and lift coefficient in frequency domain at *Ur* = 4.7; (c) Motion trajectory and lift coefficient time history at *Ur* = 6.2; (d) Motion trajectory and lift coefficient in frequency domain at *Ur* = 6.2; (e) Motion trajectory and lift coefficient time history at *Ur* = 8.0; (f) Motion trajectory and lift coefficient in frequency domain at *Ur* = 8.0; (g) Motion trajectory and lift coefficient time history at *Ur* = 10.8; (h) Motion trajectory and lift coefficient in frequency domain at *Ur* = 10.8; (i) Motion trajectory and lift coefficient time history at *Ur* = 14.7; (j) Motion trajectory and lift coefficient in frequency domain at *Ur* = 14.7.

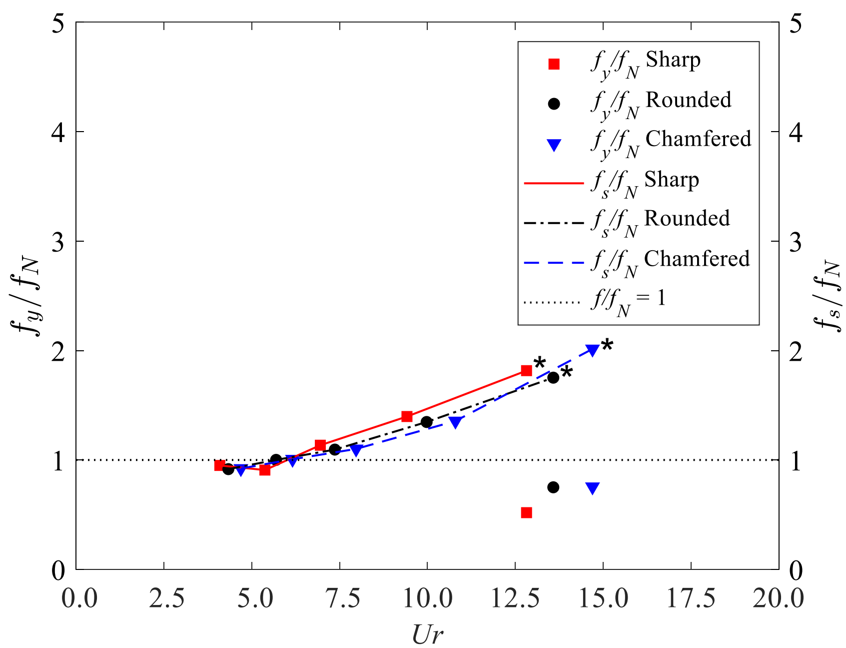


**Fig. 12** Non-dimensional transverse response frequency $f_y/f_N$ and non-dimensional vortex shedding frequency $f_s/f_N$ (* is the secondary peak observed in the frequency domain for $f_y/f_N$).

**Fig. 13**, **Fig. 14** and **Fig. 15** show the motion trajectories in the *XY* plane for the structure with different corner designs. Similar to a single cylinder, a typical “8” shaped trajectory is observed in the present study for all corner designs in the “lock-in” region. In the “post lock-in” region, the motion trajectory becomes more chaotic, especially after *Ur* = 10. For the chamfered corner design, it is observed that the transverse motion amplitude is approximately 2.4% higher than the resonance motion amplitude (at *Ur* = 6.2) in the "lock-in" region. The galloping at 45° incidence for a square-section shape column was observed when the corner shape modified as a chamfered corner.

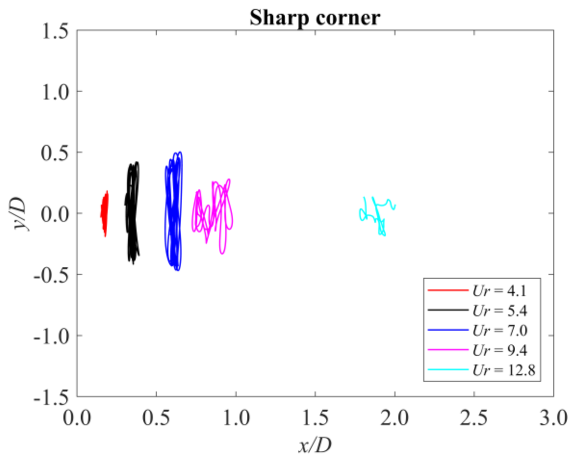


**Fig. 13** Motion trajectories in the *XY* plane for the sharp corner design.

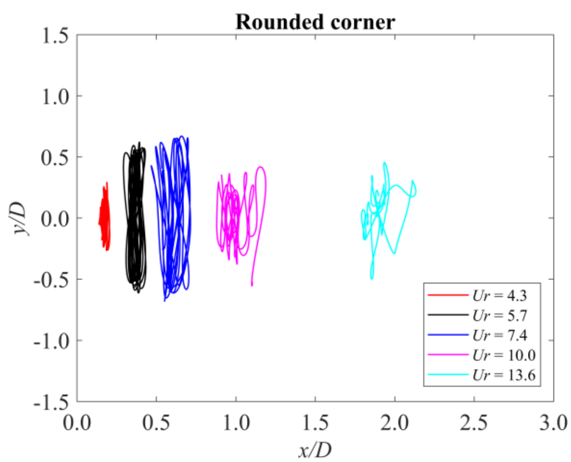


**Fig. 14** Motion trajectories in the *XY* plane for the rounded corner design.

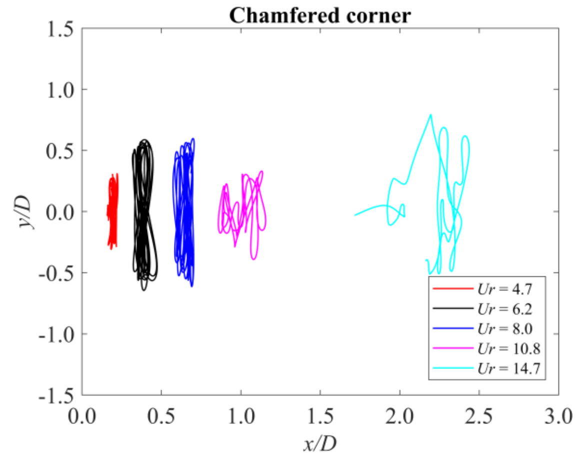


**Fig. 15** Motion trajectories in the *XY* plane for the chamfered corner design.

4.2.4. Energy transformation during the vortex shedding process

The phase angle ($\emptyset_{C_L\text{-}A_y/L}$) between the lift coefficient and transverse motion amplitude, calculated based on the averaged time lag between the local maximum points of lift coefficient and the transverse motion amplitude, is presented in **Fig. 16**. In the present study, more than fifteen cycles of the VIM transverse oscillation period are considered for time averaging. The averaged time lag is then multiplied with the frequency of vortex shedding to estimate the phase angle. As seen in **Fig. 16**, the phase angles in the "pre lock-in" and "lock-in" region are close to zero, and then begin to increase in the "post lock-in" region. After $Ur \approx 10$, the phase angle reaches approximately 180º followed by a rapid decreasing for the sharp and rounded corner designs, indicating a rapid decrease in the transverse motion response. Unlike the sharp and rounded corner designs, a distinct increasing trend of the phase angle is observed along with the reduced velocity for the chamfered corner design, and reaches around 220º at $Ur = 14.7$. This increment signifies the large transverse amplitude in the "post lock-in" region for the chamfered corner design.

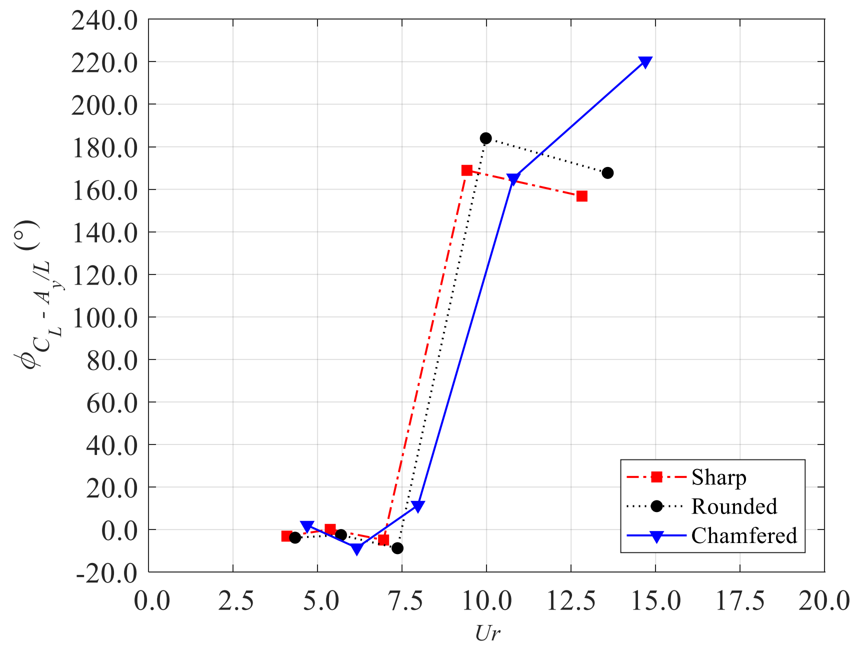


**Fig. 16** Phase angle between lift coefficient and transverse amplitude.

To examine the complex energy transformation to the structure and the corresponding motion driven parts of the structures, the lift force coefficients and work done on different structure members are further calculated and presented in **Fig. 17**. As seen in **Fig. 17** (a), for a sharp corner design, all the members of the structure are excited due to the "lock-in" phenomenon. However, when the corners are modified as a rounded shape (**Fig. 17** (b)), the leading upstream column (Column 1) shows a different trend. The lift coefficient on the upstream column is seen to decrease while an increasing trend is observed for the other members. By changing the corner shape to chamfered, the lift coefficient on the portside column (Column 2) and the starboard side column (Column 4) shows a different trend compared with other members of the structure (**Fig. 17** (c)). None resonance has been observed on the two side columns. Other members (Column 1, Column 3 and pontoons) are excited by the "lock-in" phenomenon. Apart from the force distributions, a straightforward routine to examine the contribution of each member to VIM is to determine the work done during the VIM for each member, and the work done by each member of the structure is shown in **Fig. 17**. The symmetrical characteristics can be clearly identified for all corner design. In addition to the findings made from the previous study[13], the following new insights can be revealed:

1. Resonance of the work done by the two side columns can be observed for all designs in the present study. However, the resonance is absent to the lift force on the two side columns. Further, for the chamfered corner design, no resonance is observed in both the work done and the lift force in the current study.

2. The work done by the pontoons is highly related to the transverse motion. The pontoon reduces the VIM response throughout the reduced velocity range. In addition, as the transverse motion being more severe, the effect is stronger for the pontoons to restrain the motion in the "lock-in" region.

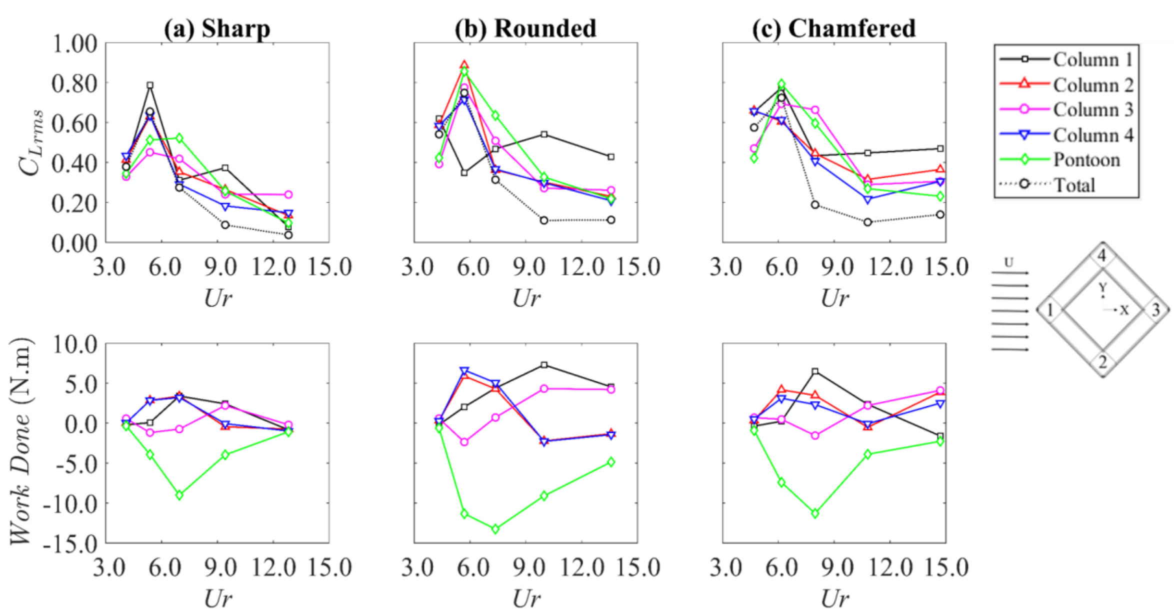


**Fig. 17** Root mean square lift coefficient ($C_{Lrms}$) and work done on each member of the structure. (a) sharp corner design; (b) rounded corner design; (c) chamfered corner design.

As seen in **Fig. 9**, **Fig. 10** and **Fig. 11**, in the “pre lock-in” and “lock-in” region, the motion response frequency ($f_y$) and vortex shedding frequency ($f_s$) are both well located around the natural frequency of the structure. This indicates a pure energy transfer from the vortex shedding to the VIM motion of the structure. However, when it shifts to the “post lock-in” region, the motion response frequency ($f_y$) and vortex shedding frequency ($f_s$) start to show a different trend with the vortex shedding frequency ($f_s$) increasing to a higher level while two peaks appearing in the motion responses frequency ($f_y$) domain. This indicates a more complex energy transformation between the flow and the structure.

In addition to the phase angle and work done analysis, to provide time-series analysis that can reveal some energy transformation process in the dynamic system, the vortex-induced motions were analysed with continuous wavelet transform (CWT). The CWT provides temporally resolved frequency analysis to give insight into the dynamics of VIM through the time traces in the “post lock-in” region. As seen in **Fig. 18**, the dominant vortex shedding frequency ($f_s$) for a sharp corner design is nearly two times of the natural frequency of the structure ($f_N$). It can be observed that the energy existed during the VIM is relatively low when compared with the other two corner shape designs. This also indicates the extremely small transverse amplitude of the structure. By modifying the corner shape to a rounded corner, the energy contours based on continuous wavelet transform are altered significantly as shown in **Fig. 19**. It can be seen that, the vortex shedding frequency ($f_s$) fluctuates around two times of the natural frequency of the structure ($f_N$). The motion response frequency ($f_y$) is equally distributed around the natural frequency of the structure ($f_N$) and at two times of $f_N$. In parts of the time series, these two equally weighted frequency can be merged together leading to a high energy density as shown in **Fig. 19**. When the corner shape changed to a chamfered one, further considerable change can be observed for the energy contours shown in **Fig. 20**. The vortex shedding frequency increases to a higher level where the highest vortex shedding frequency can reach up to more than 3 times of the structural natural frequency ($f_N$). However, the majority of the energy in the transverse motion response is located at the frequency range lower than the natural frequency ($f_N$). This indicates the development of the galloping phenomenon. In addition, the energy density of the chamfered corner is much higher than the other two corner shape designs.

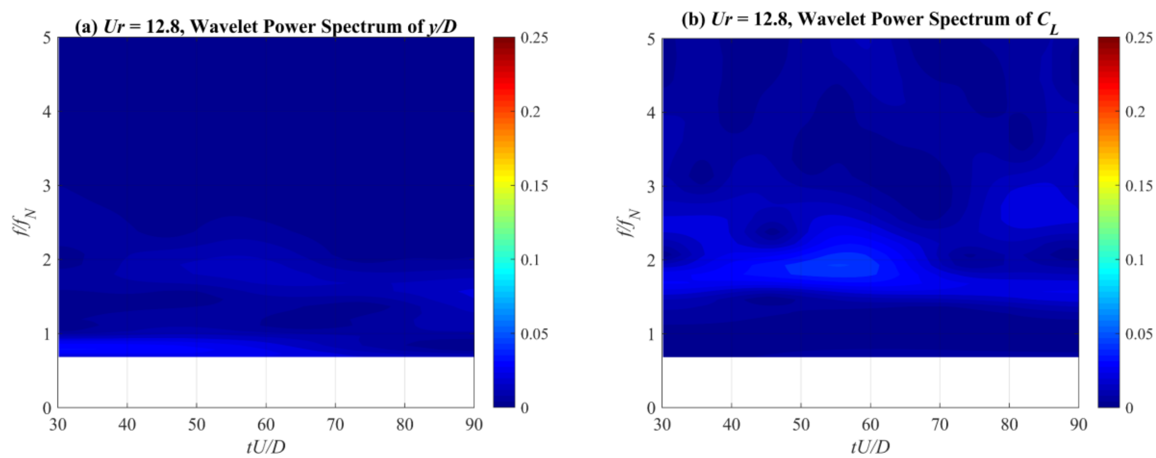


**Fig. 18** Time series of the non-dimensional (a) transverse motion response frequency and (b) vortex shedding frequency with the frequency energy contours based on continuous wavelet transforms in the "post lock-in" region for a sharp corner design.

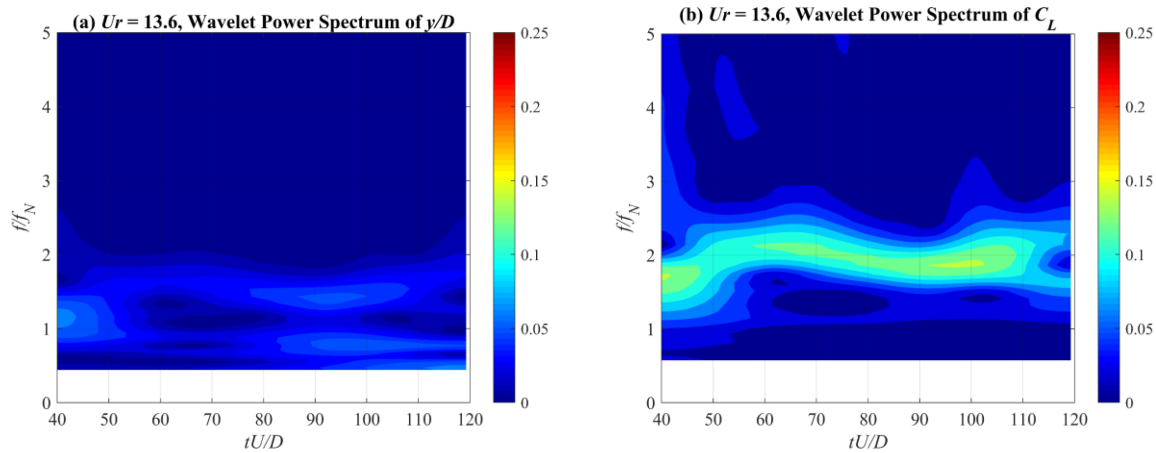


**Fig. 19** Time series of the non-dimensional (a) transverse motion response frequency and (b) vortex shedding frequency with the frequency energy contours based on continuous wavelet transforms in the "post lock-in" region for a rounded corner design.

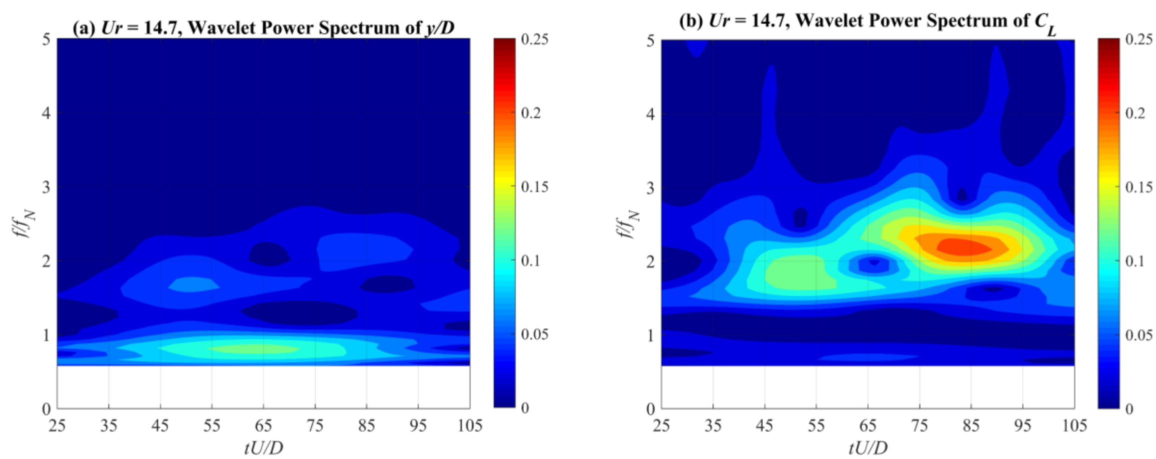


**Fig. 20** Time series of the non-dimensional (a) transverse motion response frequency and (b) vortex shedding frequency with the frequency energy contours based on continuous wavelet transforms in the "post lock-in" region for a chamfered corner design.

### 4.3. Flow patterns

#### 4.3.1. Instantaneous vorticity and streamline

In order to have a general visual appreciation of the vortex shedding patterns, the vorticity contours with instantaneous streamlines in the "lock-in" region are plotted in **Fig. 21**. The non-dimensional spanwise vorticity is used to describe the vorticity in the present work:

$$\textit{non-dimensional spanwise vorticity} = \vec{\omega}_z D/U,, \qquad (11)$$

where, $\vec{\omega}_z$ is the $z$ component of the vorticity, $D$ is the projected length of the column and $U$ is the current speed.

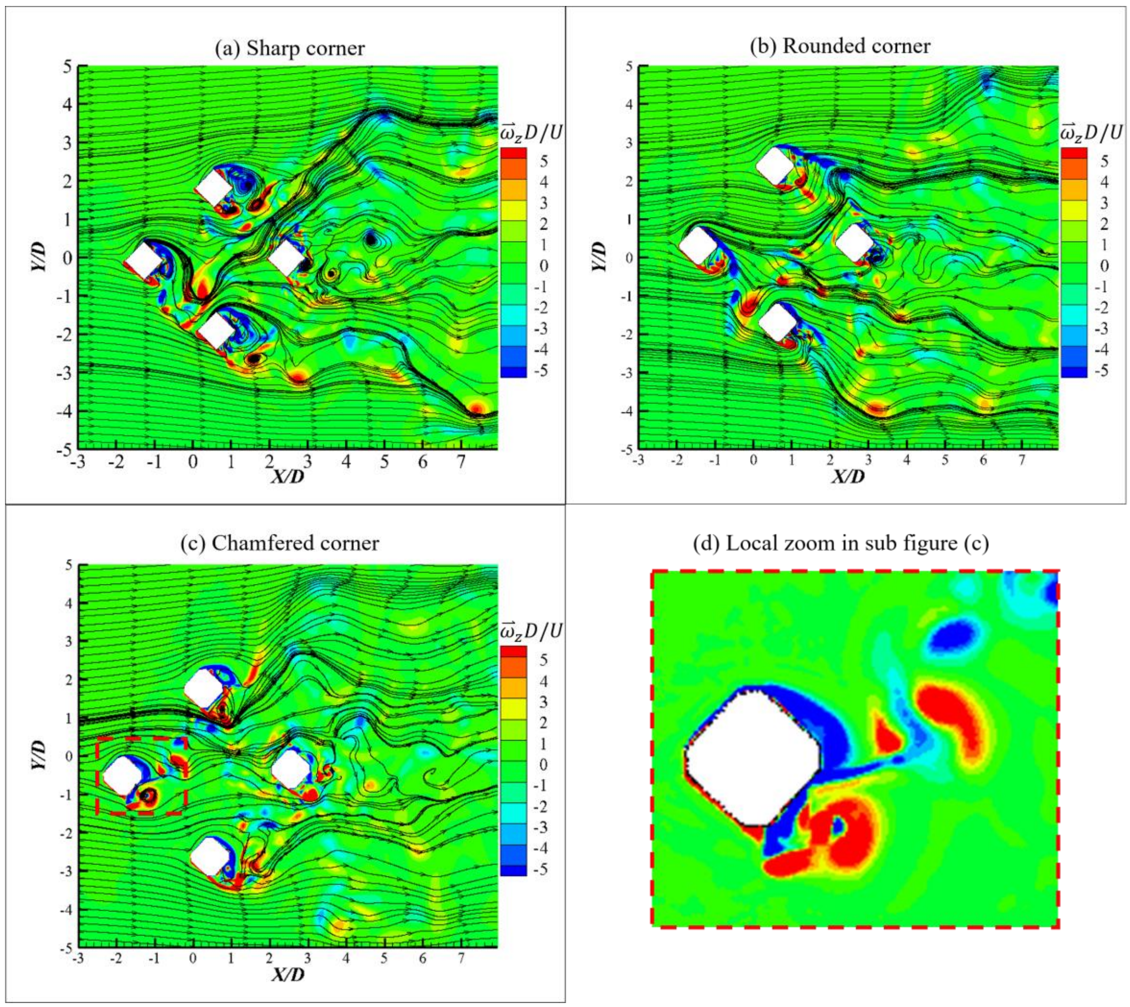


**Fig. 21** Instantaneous vorticity contours and streamline for different corner designs. (a) sharp corner design; (b) rounded corner design; (c) chamfered corner design; (d) a local zoom vorticity contour in (c).

As seen in **Fig. 21**, the vortices shed from the upstream corner are finally separated from the side column for both sharp and rounded corner. However, for a chamfered corner shape design case, a unique “re-attached vortex shedding” phenomenon is observed in **Fig. 21** (d). The vortices shed from the upstream corner of the column will be separated at one side of the column. However, due to the large amplitude transverse motion and the corner design, it will be “re-attached” to the downstream corner of the column and further reaching to the other side corner of the column. This indicates a higher vortex shedding frequency within one dominated vortex shedding period for the overall structure as shown in **Fig. 11**(b). This “re-attached” phenomenon has been only observed for the chamfered corner case at the “lock-in” region. It is noted that the energy of this high frequency “re-attach vortex shedding” is extremely small compared with the overall vortex shedding frequency.

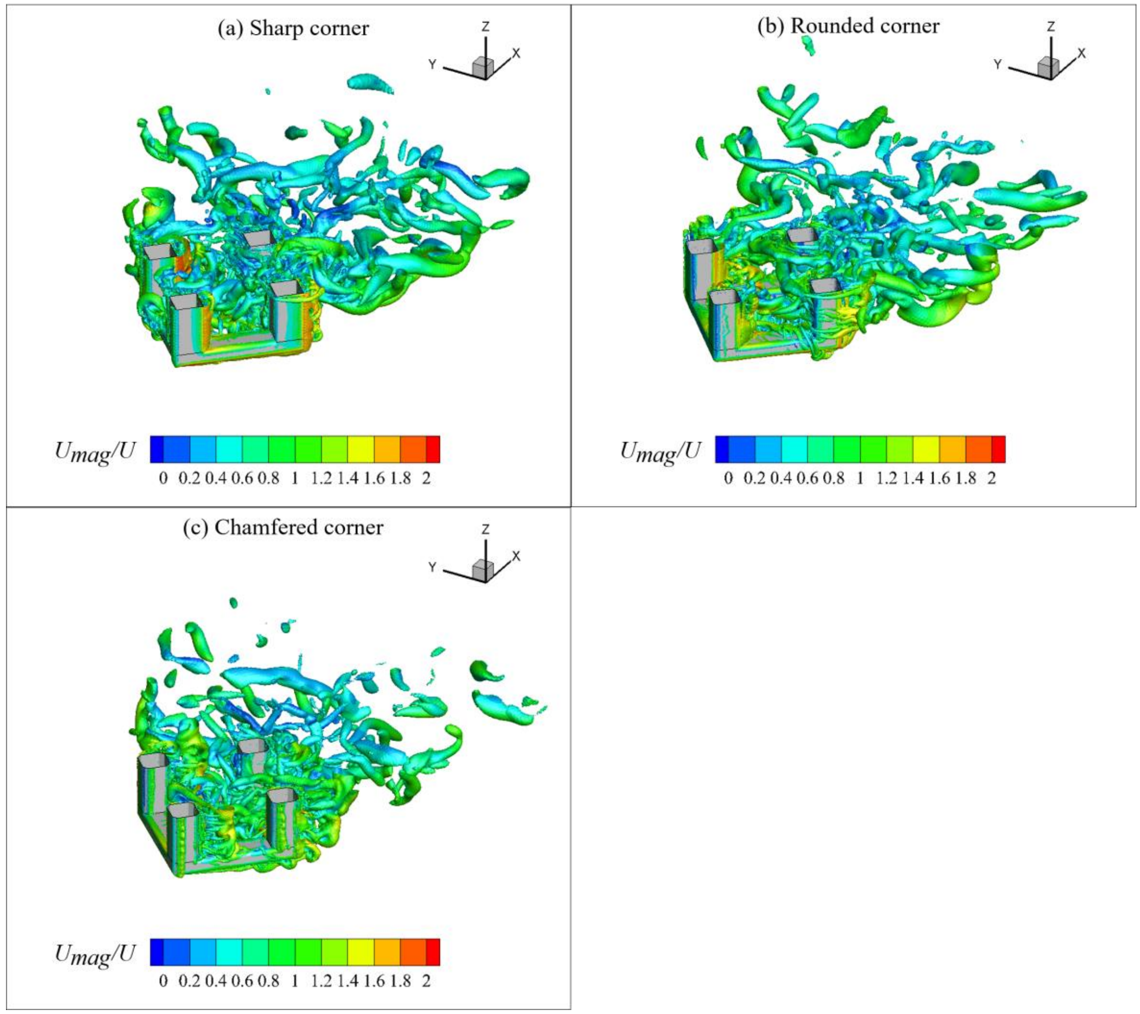


**Fig. 22** Isometric view representation of *Q*-criterion of the three different corner design covered by the non-dimensional velocity contours. (a) sharp corner design; (b) rounded corner design; (c) chamfered corner design.

To further understand the structures of the wake regions associated with the three different corner shape designs, a vortex identification method based on the *Q*-criterion has been employed in the present study. **Fig. 22** presents the *Q*-criterion based vertical structures for the three corner designs. The isofurfaces are shown at a constant positive value where $Q = 0.1$ and covered by the non-dimesnional velocity contours. It can be clearly seen that the sharp corner design only has a single separation point at the upstream corner while the chamfered corner design has two separation points at the upstream corner.

## 4. Conclusions

This paper presents a numerical study focusing on the energy transformation on flow-induced motions of multiple cylindrical structures with various corner shapes. Three different corner shapes were considered, i.e. sharp, rounded and chamfered. The differences of the flow characteristics, the hydrodynamic forces as well as the motion responses are investigated. Based on the relationship between the hydrodynamic forces and the motion responses, the energy transformation between the flow and the structure are further discussed in a perspective of phase angle, work done and frequency energy contours.

By examing the characteristics mentioned above, a galloping at 45° incidence for a square-section shape column is observed when the corner shape modified as a chamfered corner. In addition, a “re-attached vortex shedding” phenomenon is identified when the “lock-in” happened for a chamfered corner design. The cause of this phenomenon is explained by the instantaneous vorticity contours presented in the current study.

The analysis of the energy transformation between the flow and the structure revealed that modifying the corner shape had a large effect on the energy transformation leading to a significant change in the hydrodynamic forces and the FIM motion responses.

This study focuses on the 45 degree flow incidence, hence more incidences should be considered and examined in order to obtain a more generalized understanding of the energy transformation process during FIM of a multi-column floating structure.

## Acknowledgement

The authors would like to acknowledge the support of Newton Fund of Royal Academy of Engineering UK (NRCP/1415/211). This work made use of the facilities of N8 HPC Centre of Excellence, provided and funded by the N8 consortium and EPSRC (Grant No.EP/K000225/1).

## References

1. T. Kokkinis, R. E. Sandström, H. T. Jones, H. M. Thompson, and W. L. Greiner, *Development of a Stepped Line Tensioning Solution for Mitigating VIM Effects in Loop Eddy Currents for the Genesis Spar* (American Society of Mechanical Engineers, 2004).
2. A. L. C. Fujarra, G. F. Rosetti, J. de Wilde, and R. T. Gonçalves, *State-of-art on vortex-induced motion: a comprehensive survey after more than one decade of experimental investigation* (American Society of Mechanical Engineers, 2012).
3. O. J. Waals, A. C. Phadke, and S. Bultema, *Flow Induced Motions on Multi Column Floaters* (American Society of Mechanical Engineers, 2007).
4. O. Rijken, and S. Leverette, *Field measurements of vortex induced motions of a deep draft semisubmersible* (American Society of Mechanical Engineers, 2009).
5. J. Den Hartog, "Transmission line vibration due to sleet," Transactions of the American Institute of Electrical Engineers **51**, 1074 (1932).
6. B. Liu, and R. K. Jaiman, "Interaction dynamics of gap flow with vortex-induced vibration in side-by-side cylinder arrangement," Physics of Fluids **28**, 127103 (2016).
7. Z. Li, R. K. Jaiman, and B. C. Khoo, "Coupled dynamics of vortex-induced vibration and stationary wall at low Reynolds number," Physics of Fluids **29**, 093601 (2017).
8. W. Yao, and R. Jaiman, "Stability analysis of the wake-induced vibration of tandem circular and square cylinders," Nonlinear Dynamics **95**, 13 (2019).

9. L. Shen, and Z. Sun, "Jump phenomena in vortex-induced vibrations of a circular cylinder at a low Reynolds number," Physics of Fluids **31**, 123605 (2019).
10. H. Zhu, C. Zhang, and W. Liu, "Wake-induced vibration of a circular cylinder at a low Reynolds number of 100," Physics of Fluids **31**, 073606 (2019).
11. H. Jiao, and G. Wu, "Free vibration predicted using forced oscillation in the lock-in region," Physics of Fluids **30**, 113601 (2018).
12. M. Rastan, A. Sohankar, and M. M. Alam, "Low-Reynolds-number flow around a wall-mounted square cylinder: Flow structures and onset of vortex shedding," Physics of Fluids **29**, 103601 (2017).
13. Y. Liang, and L. Tao, "Interaction of vortex shedding processes on flow over a deep-draft semi-submersible," Ocean Engineering **141**, 427 (2017).
14. Y. Liang, L. Tao, L. Xiao, and M. Liu, "Experimental and numerical study on vortex-induced motions of a deep-draft semi-submersible," Applied Ocean Research **67**, 169 (2017).
15. P. W. Bearman, J. M. R. Graham, E. D. Obasaju, and G. M. Drossopoulos, "The influence of corner radius on the forces experienced by cylindrical bluff bodies in oscillatory flow," Applied Ocean Research **6**, 83 (1984).
16. J. C. Hu, Y. Zhou, and C. Dalton, "Effects of the corner radius on the near wake of a square prism," Experiments in Fluids **40**, 106 (2005).
17. M. Liu, L. Xiao, J. Yang, and X. Tian, "Parametric study on the vortex-induced motions of semi-submersibles: Effect of rounded ratios of the column and pontoon," Physics of Fluids **29**, 055101 (2017).
18. T. Tamura, T. Miyagi, and T. Kitagishi, "Numerical prediction of unsteady pressures on a square cylinder with various corner shapes," Journal of Wind Engineering and Industrial Aerodynamics **74**, 531 (1998).
19. T. Tamura, and T. Miyagi, "The effect of turbulence on aerodynamic forces on a square cylinder with various corner shapes," Journal of Wind Engineering and Industrial Aerodynamics **83**, 135 (1999).
20. Y. Cao, and T. Tamura, "Supercritical flows past a square cylinder with rounded corners," Physics of Fluids **29**, 085110 (2017).

21. J. Zhao, A. Nemes, D. Lo Jacono, and J. Sheridan, "Branch/mode competition in the flow-induced vibration of a square cylinder," Philosophical Transactions of the Royal Society A: Mathematical, Physical and Engineering Sciences **376**, 20170243 (2018).
22. J. Zhao, J. S. Leontini, D. L. Jacono, and J. Sheridan, "Fluid–structure interaction of a square cylinder at different angles of attack," Journal of Fluid Mechanics **747**, 688 (2014).
23. R. T. Gonçalves, G. F. Rosetti, A. L. C. Fujarra, and A. C. Oliveira, "Experimental study on vortex-induced motions of a semi-submersible platform with four square columns, Part I: Effects of current incidence angle and hull appendages," Ocean Engineering **54**, 150 (2012).
24. A. Antony, V. Vinayan, S. Madhavan, A. Parambath, J. Halkyard, J. Sterenborg, S. Holmes, D. Spernjak, S. J. Kim, and W. Head, *VIM Model Test of Deep Draft Semisubmersibles Including Effects of Damping* (Offshore Technology Conference, 2016).
25. Y. Liang, and L. Tao, "Interaction of vortex shedding processes on flow over a deep-draft semi-submersible," Ocean Engineering (2017).
26. G. Schewe, "On the force fluctuations acting on a circular cylinder in crossflow from subcritical up to transcritical Reynolds numbers," Journal of Fluid Mechanics **133**, 265 (1983).
27. C. Norberg, "Flow around rectangular cylinders: pressure forces and wake frequencies," Journal of wind engineering and industrial aerodynamics **49**, 187 (1993).
28. T. Sarpkaya, "A critical review of the intrinsic nature of vortex-induced vibrations," Journal of Fluids and Structures **19**, 389 (2004).
29. R. T. Gonçalves, G. F. Rosetti, A. L. C. Fujarra, and A. C. Oliveira, "Experimental study on vortex-induced motions of a semi-submersible platform with four square columns, Part II: Effects of surface waves, external damping and draft condition," Ocean Engineering **62**, 10 (2013).
30. M. L. Shur, P. R. Spalart, M. K. Strelets, and A. K. Travin, "A hybrid RANS-LES approach with delayed-DES and wall-modelled LES capabilities," International Journal of Heat and Fluid Flow **29**, 1638 (2008).
31. P. R. Spalart, W. H. Jou, M. Strelets, and S. R. Allmaras, "Comments on the feasibility of LES for wings, and on a hybrid RANS/LES approach," Advances in DNS/LES **1**, 4 (1997).

32. CD-adapco, *User Guide* (Star-CCM+ Version 9.04, 2014).
33. J. Blazek, *Computational fluid dynamics: principles and applications* (Butterworth-Heinemann, 2015).
34. I. B. Celik, U. Ghia, and P. J. Roache, "Procedure for estimation and reporting of uncertainty due to discretization in CFD applications," Journal of Fluids Engineering-Transactions of the ASME **130**, (2008).

# List of Figures

# List of Tables

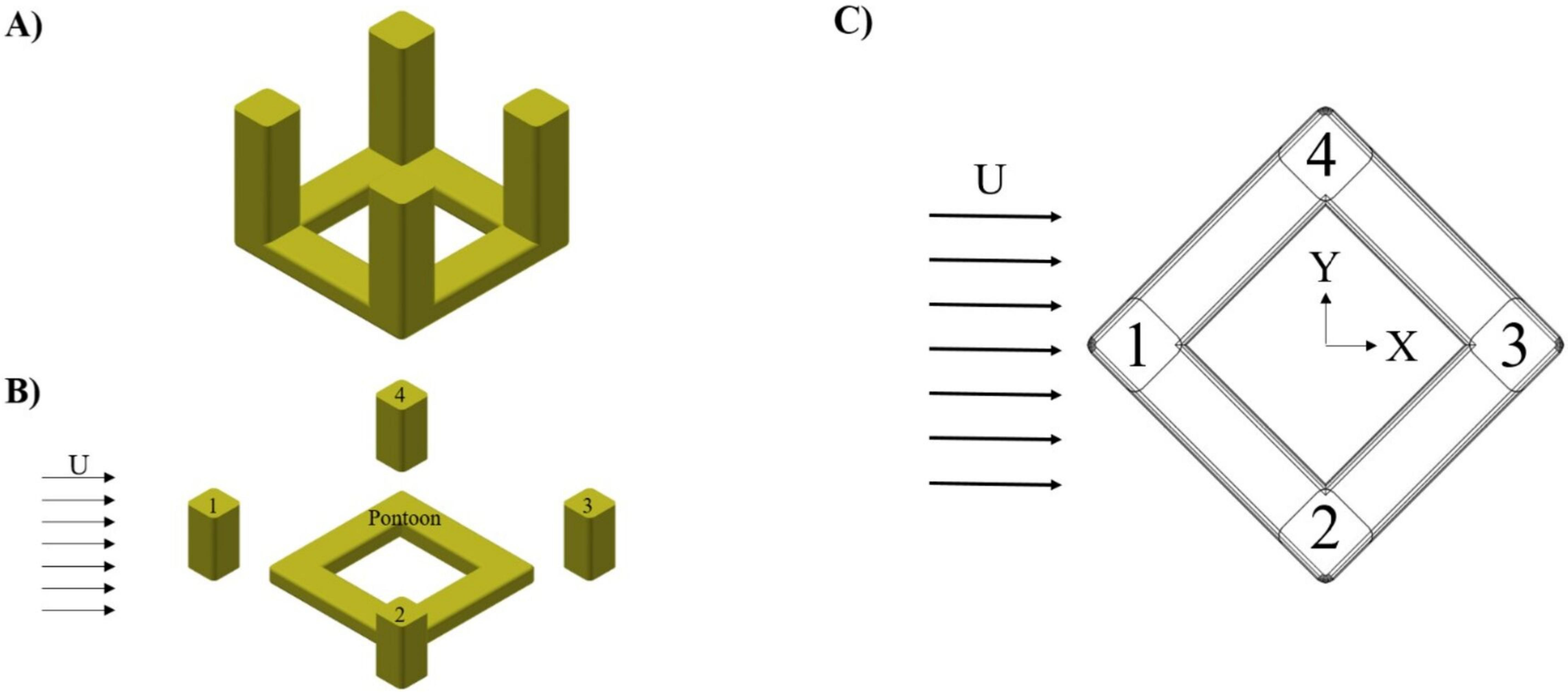

A)
B)
U
1
2
3
4
Pontoon
C)
U
1
2
3
4
Y
X

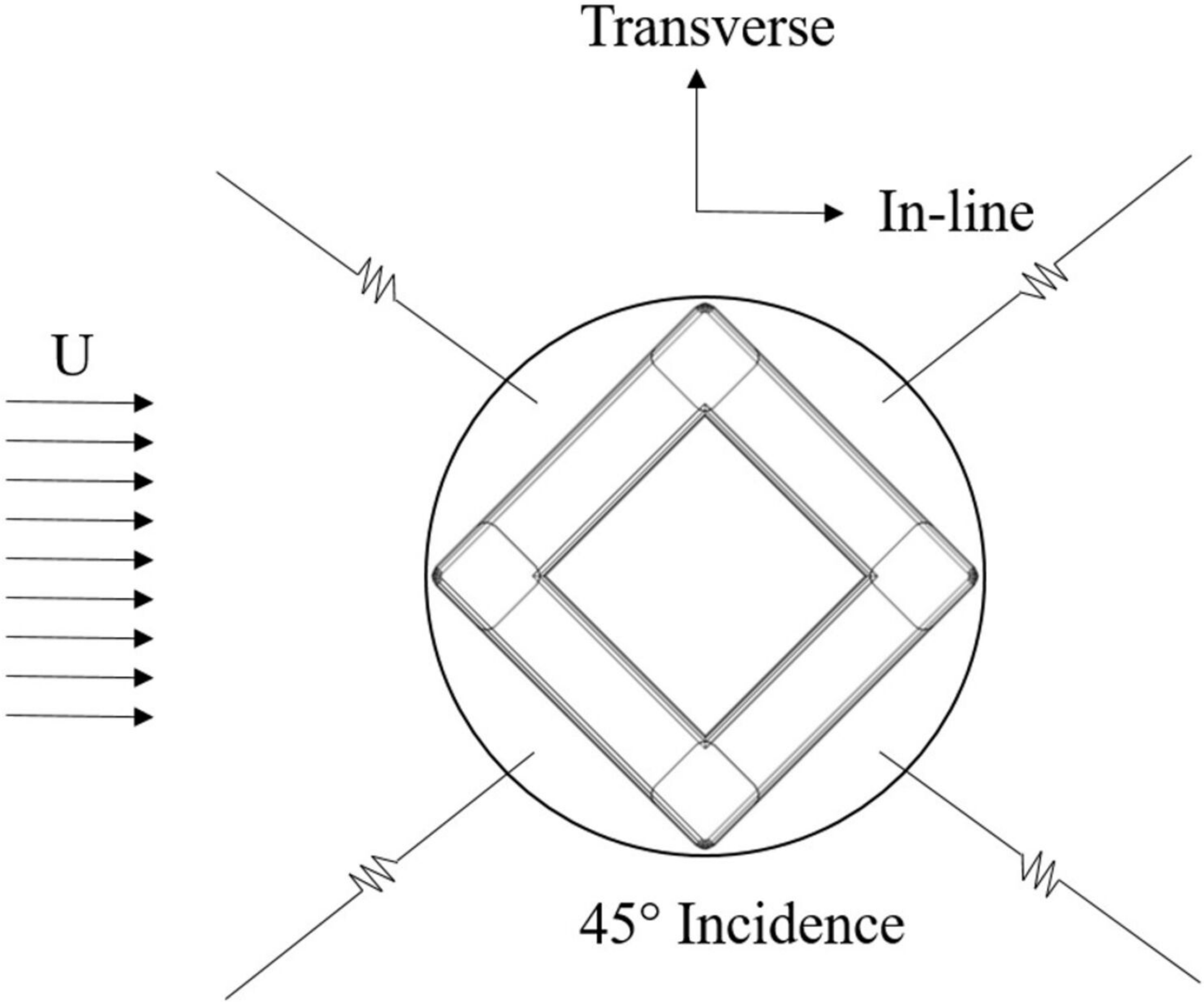
Transverse
In-line
U
45° Incidence

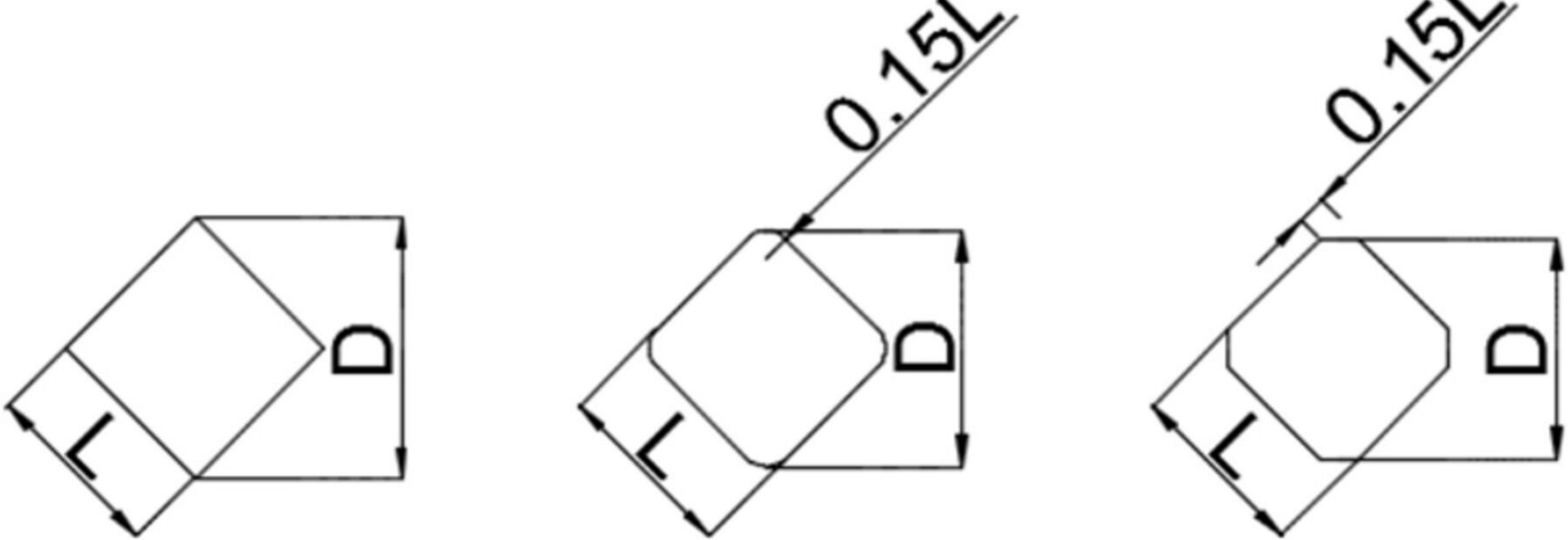


Sharp corners Rounded corners Chamfered corners

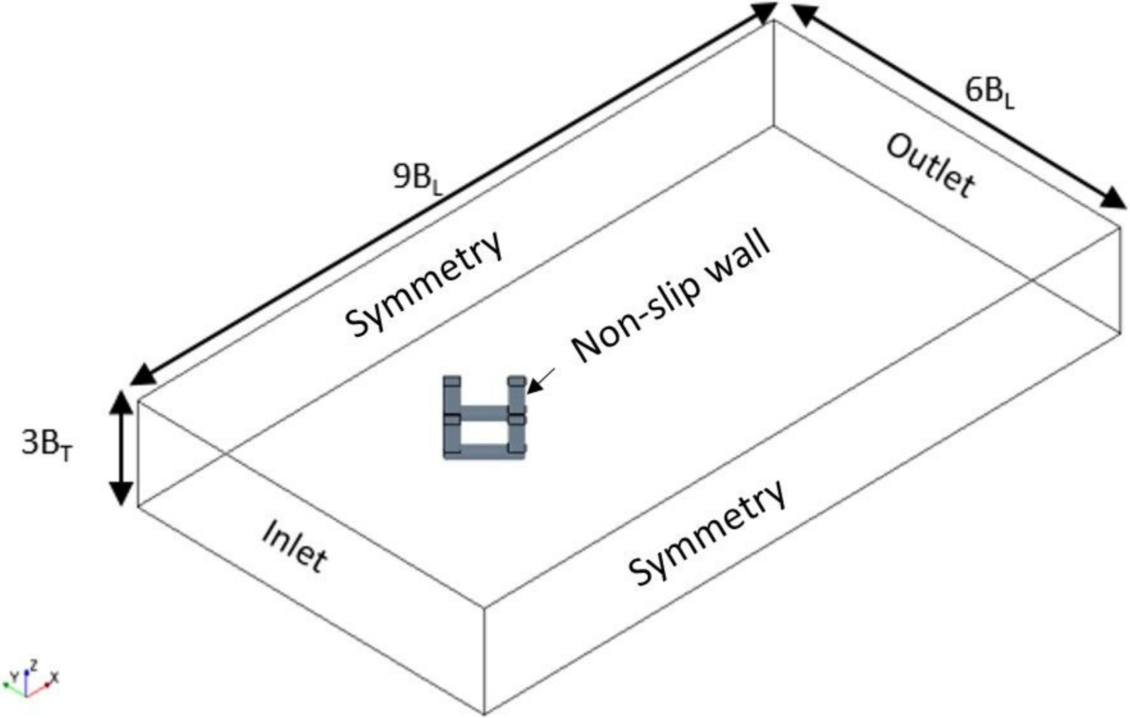

9B_L
6B_L
Outlet
Symmetry
Non-slip wall
3B_T
Inlet
Symmetry

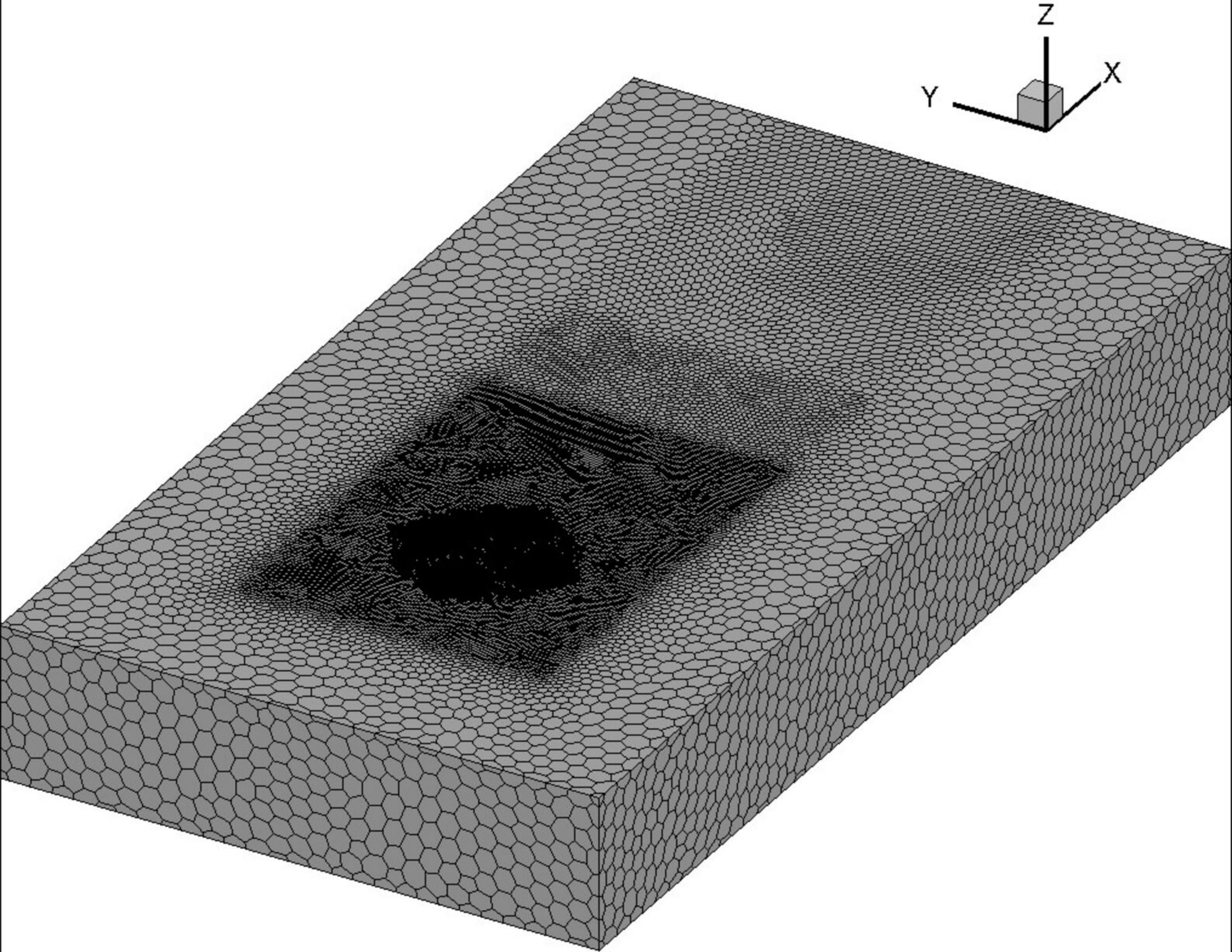
Z
Y
X

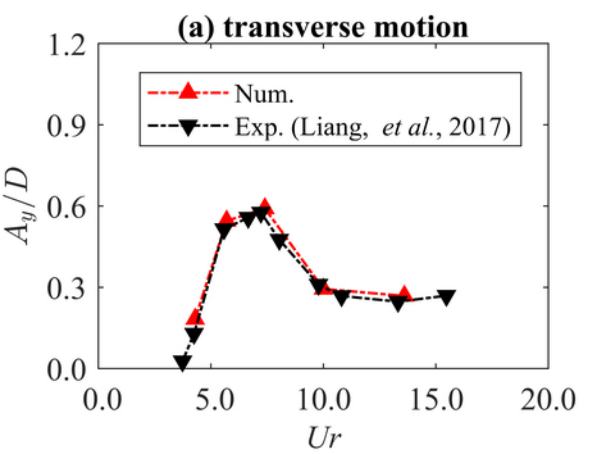

(a) transverse motion
Num.
Exp. (Liang, et al., 2017)
$A_y/D$
$Ur$
1.2
0.9
0.6
0.3
0.0
0.0
5.0
10.0
15.0
20.0

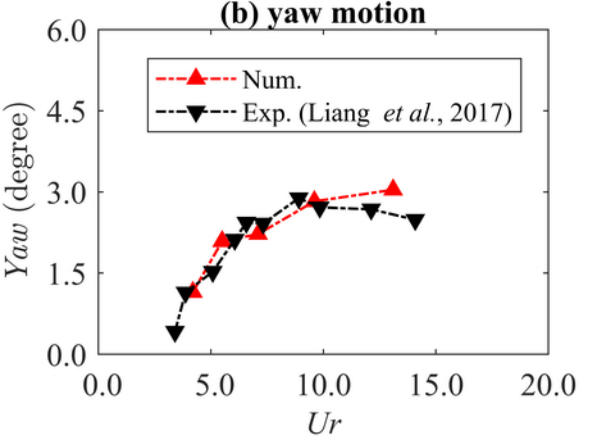

(b) yaw motion
Num.
Exp. (Liang et al., 2017)
6.0
4.5
3.0
1.5
0.0
Yaw (degree)
0.0
5.0
10.0
15.0
20.0
Ur

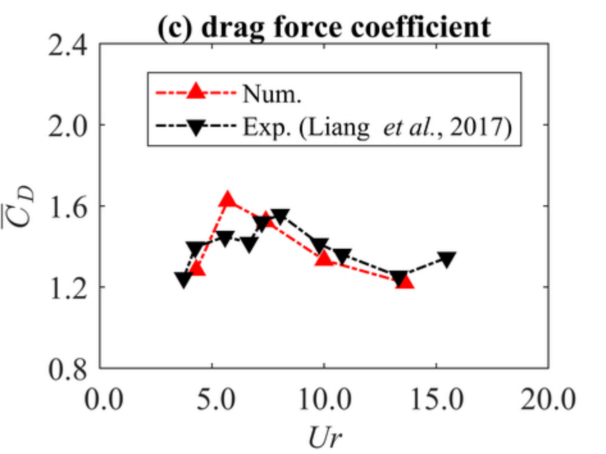
(c) drag force coefficient
Num.
Exp. (Liang et al., 2017)
$\overline{C}_D$
2.4
2.0
1.6
1.2
0.8
0.0
5.0
10.0
15.0
20.0
Ur

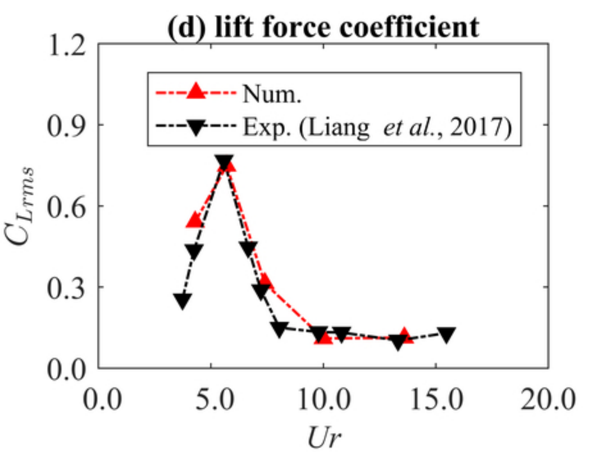
(d) lift force coefficient
1.2
0.9
0.6
0.3
0.0
$C_{Lrms}$
Num.
Exp. (Liang *et al.*, 2017)
0.0
5.0
10.0
15.0
20.0
*Ur*

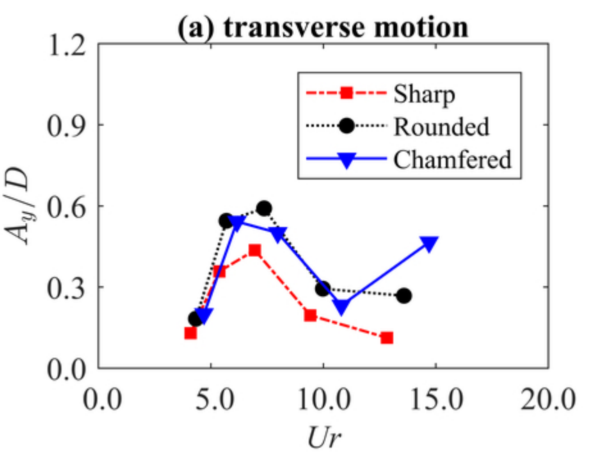

(a) transverse motion
1.2
0.9
0.6
0.3
0.0
$A_y/D$
0.0
5.0
10.0
15.0
20.0
$Ur$
Sharp
Rounded
Chamfered

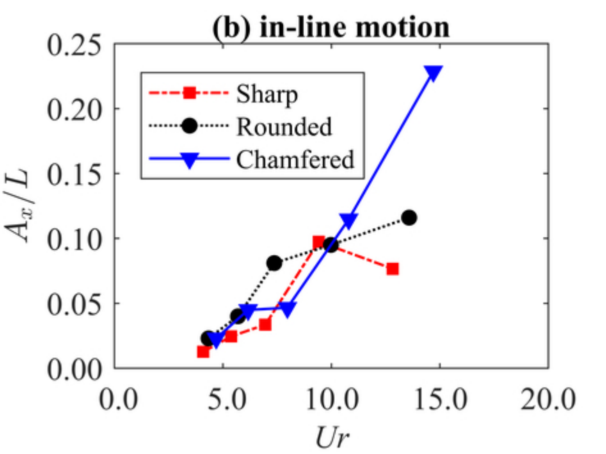

(b) in-line motion
0.25
0.20
0.15
0.10
0.05
0.00
$A_x/L$
Sharp
Rounded
Chamfered
0.0
5.0
10.0
15.0
20.0
$Ur$

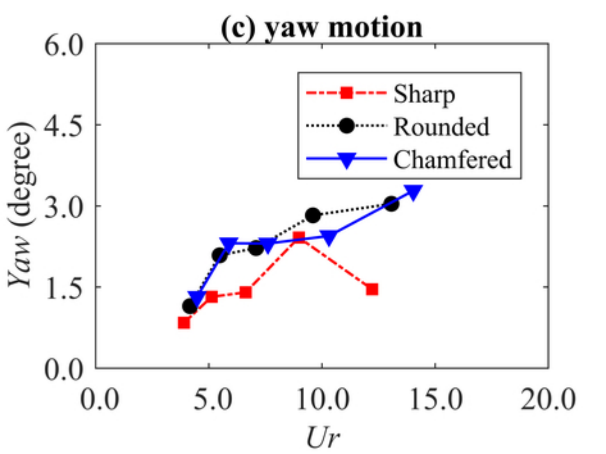
(c) yaw motion
6.0
4.5
3.0
1.5
0.0
Yaw (degree)
Sharp
Rounded
Chamfered
0.0
5.0
10.0
15.0
20.0
Ur

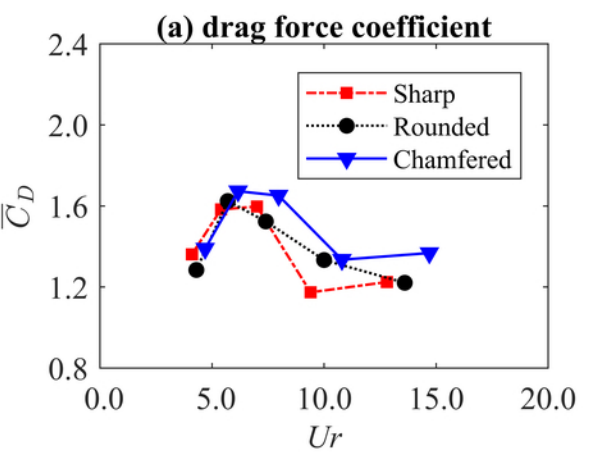

(a) drag force coefficient
Sharp
Rounded
Chamfered
2.4
2.0
1.6
1.2
0.8
$\overline{C}_D$
0.0
5.0
10.0
15.0
20.0
Ur

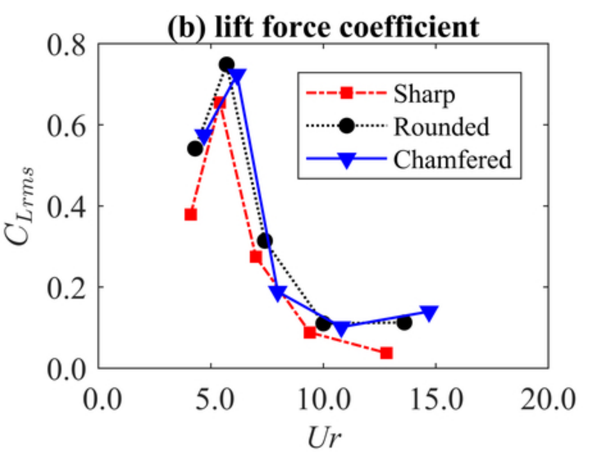

(b) lift force coefficient
0.8
0.6
0.4
0.2
0.0
$C_{Lrms}$
Sharp
Rounded
Chamfered
0.0
5.0
10.0
15.0
20.0
$Ur$

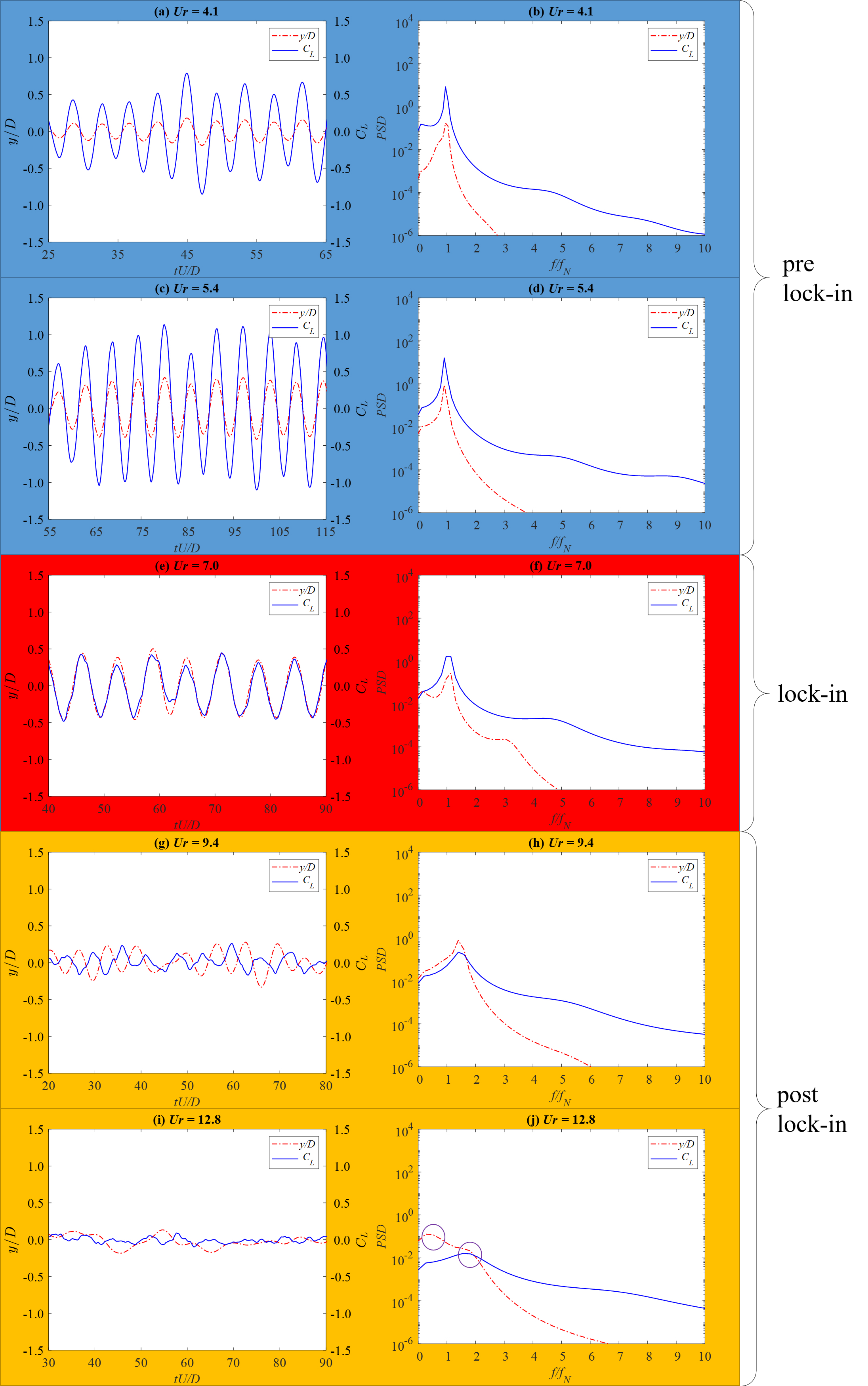

(a) Ur = 4.1
(b) Ur = 4.1
(c) Ur = 5.4
(d) Ur = 5.4
(e) Ur = 7.0
(f) Ur = 7.0
(g) Ur = 9.4
(h) Ur = 9.4
(i) Ur = 12.8
(j) Ur = 12.8
y/D
C_L
PSD
tU/D
f/f_N
pre lock-in
lock-in
post lock-in

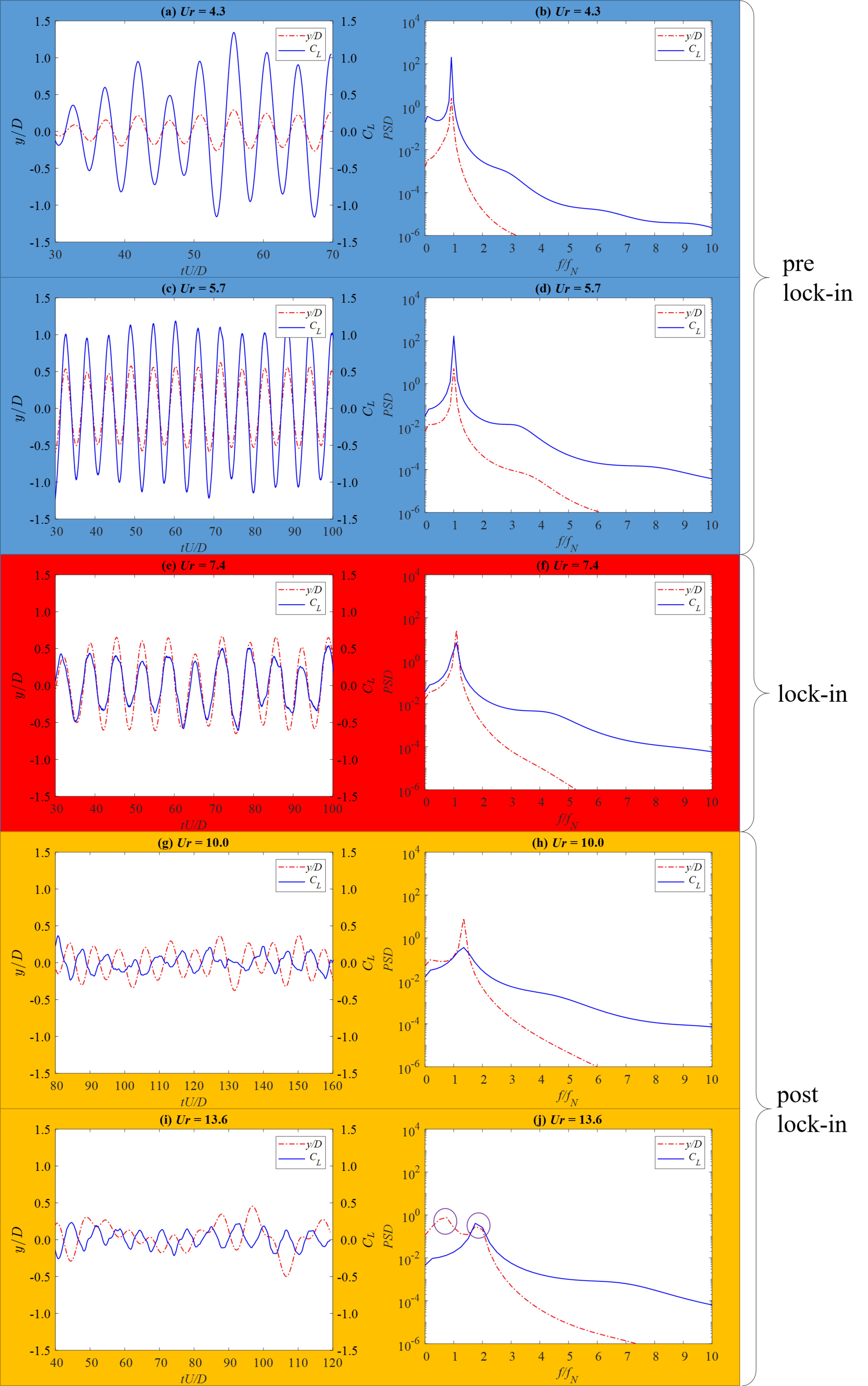
(a) Ur = 4.3
(b) Ur = 4.3
(c) Ur = 5.7
(d) Ur = 5.7
(e) Ur = 7.4
(f) Ur = 7.4
(g) Ur = 10.0
(h) Ur = 10.0
(i) Ur = 13.6
(j) Ur = 13.6
y/D
C_L
PSD
tU/D
f/f_N
pre lock-in
lock-in
post lock-in

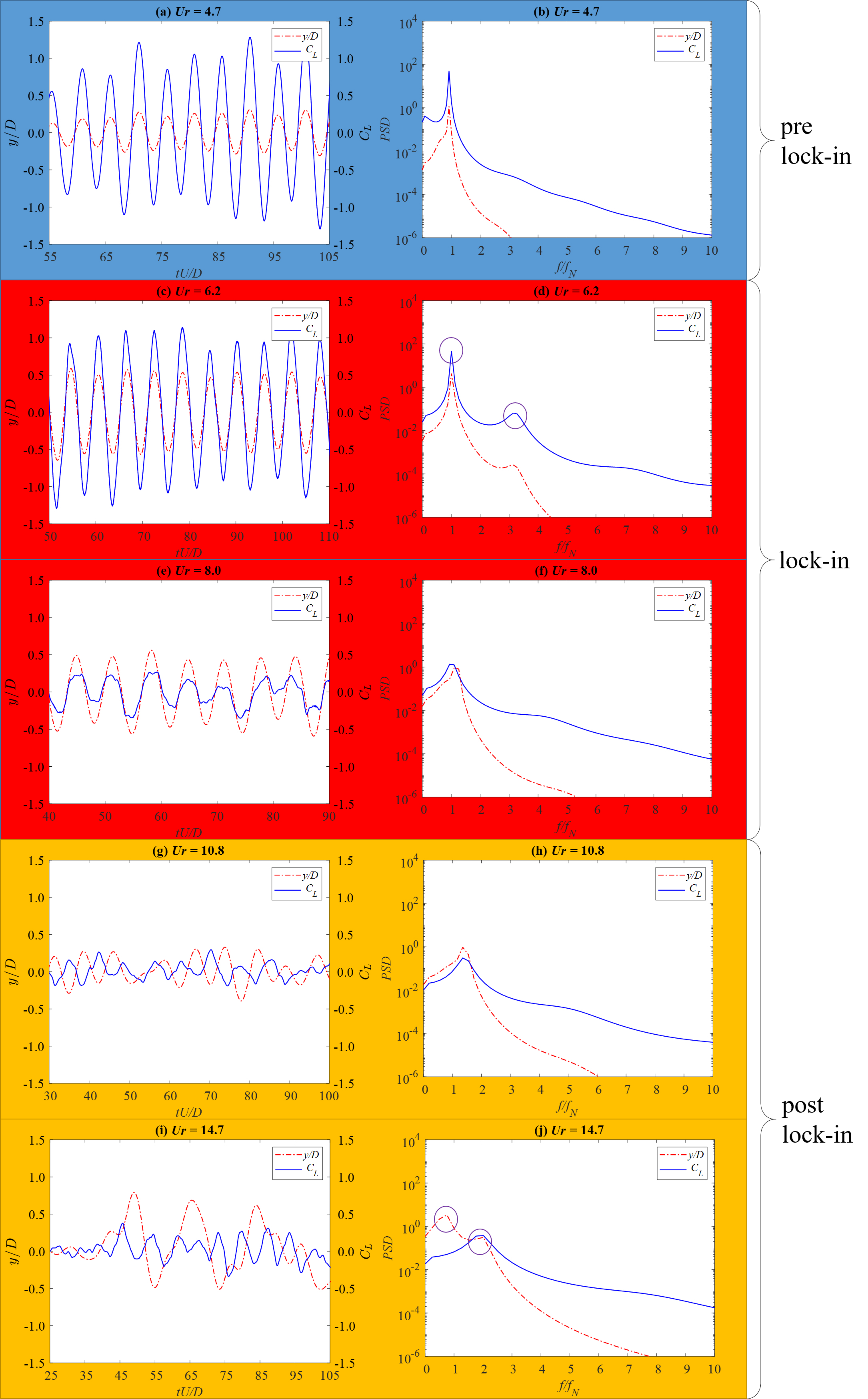

(a) Ur = 4.7
(b) Ur = 4.7
(c) Ur = 6.2
(d) Ur = 6.2
(e) Ur = 8.0
(f) Ur = 8.0
(g) Ur = 10.8
(h) Ur = 10.8
(i) Ur = 14.7
(j) Ur = 14.7
y/D
C_L
tU/D
PSD
f/f_N
pre lock-in
lock-in
post lock-in

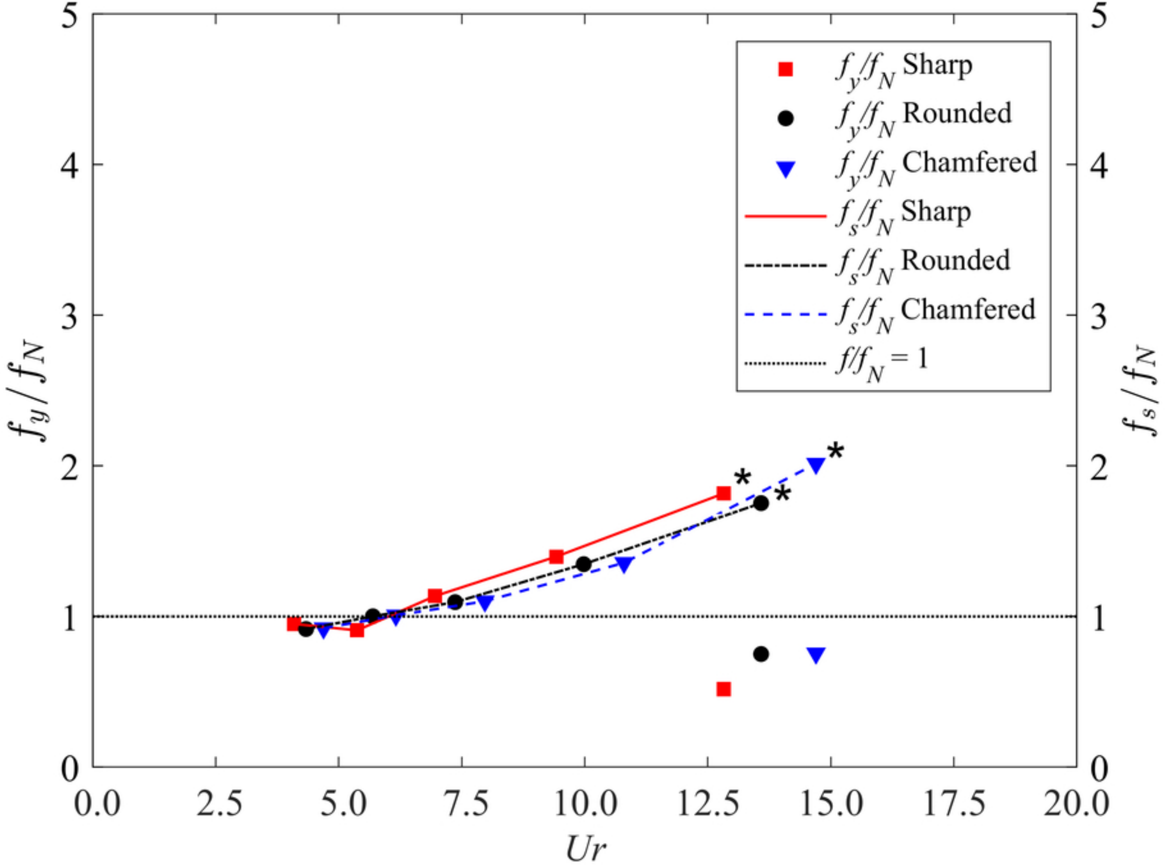

$f_y / f_N$
$f_s / f_N$
$Ur$
0.0
2.5
5.0
7.5
10.0
12.5
15.0
17.5
20.0
0
1
2
3
4
5
$f_y/f_N$ Sharp
$f_y/f_N$ Rounded
$f_y/f_N$ Chamfered
$f_s/f_N$ Sharp
$f_s/f_N$ Rounded
$f_s/f_N$ Chamfered
$f/f_N = 1$

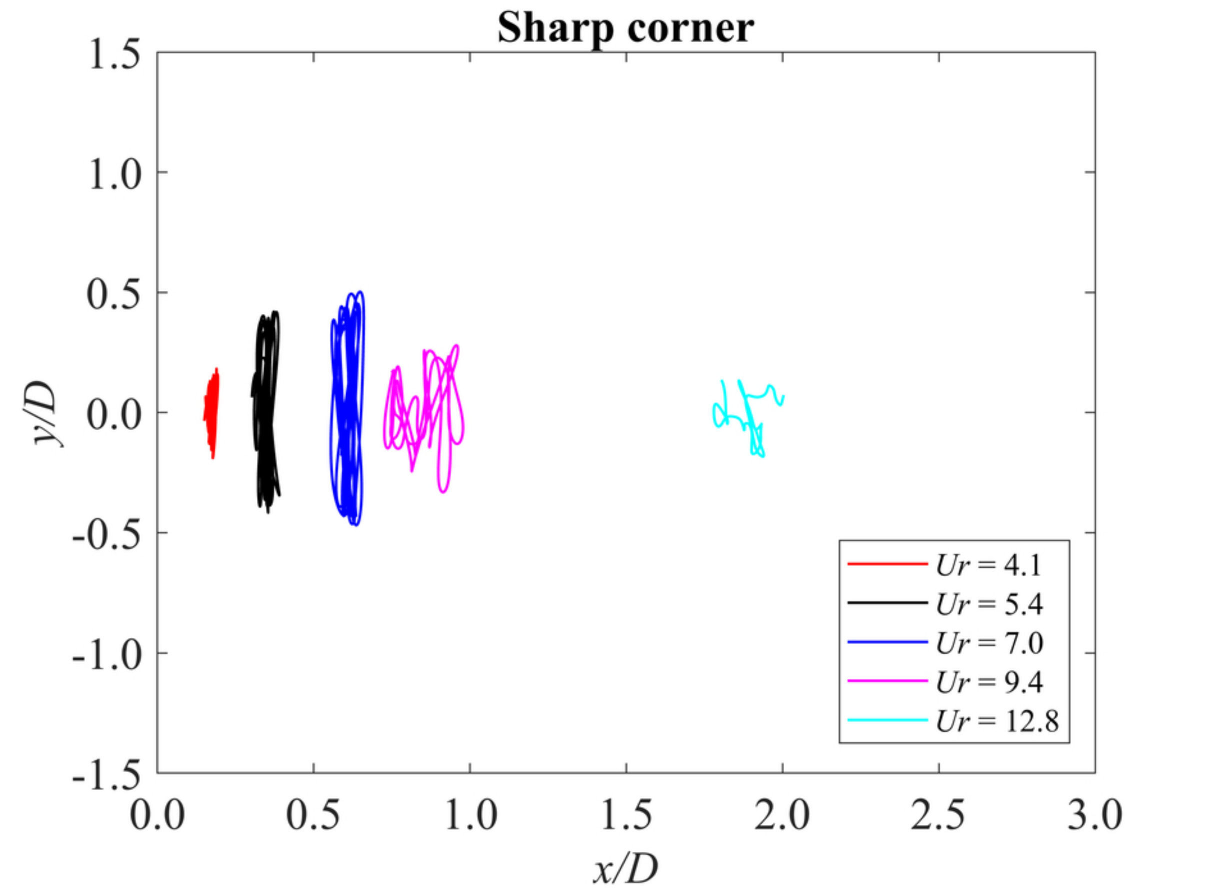
Sharp corner
1.5
1.0
0.5
0.0
-0.5
-1.0
-1.5
y/D
0.0
0.5
1.0
1.5
2.0
2.5
3.0
x/D
Ur = 4.1
Ur = 5.4
Ur = 7.0
Ur = 9.4
Ur = 12.8

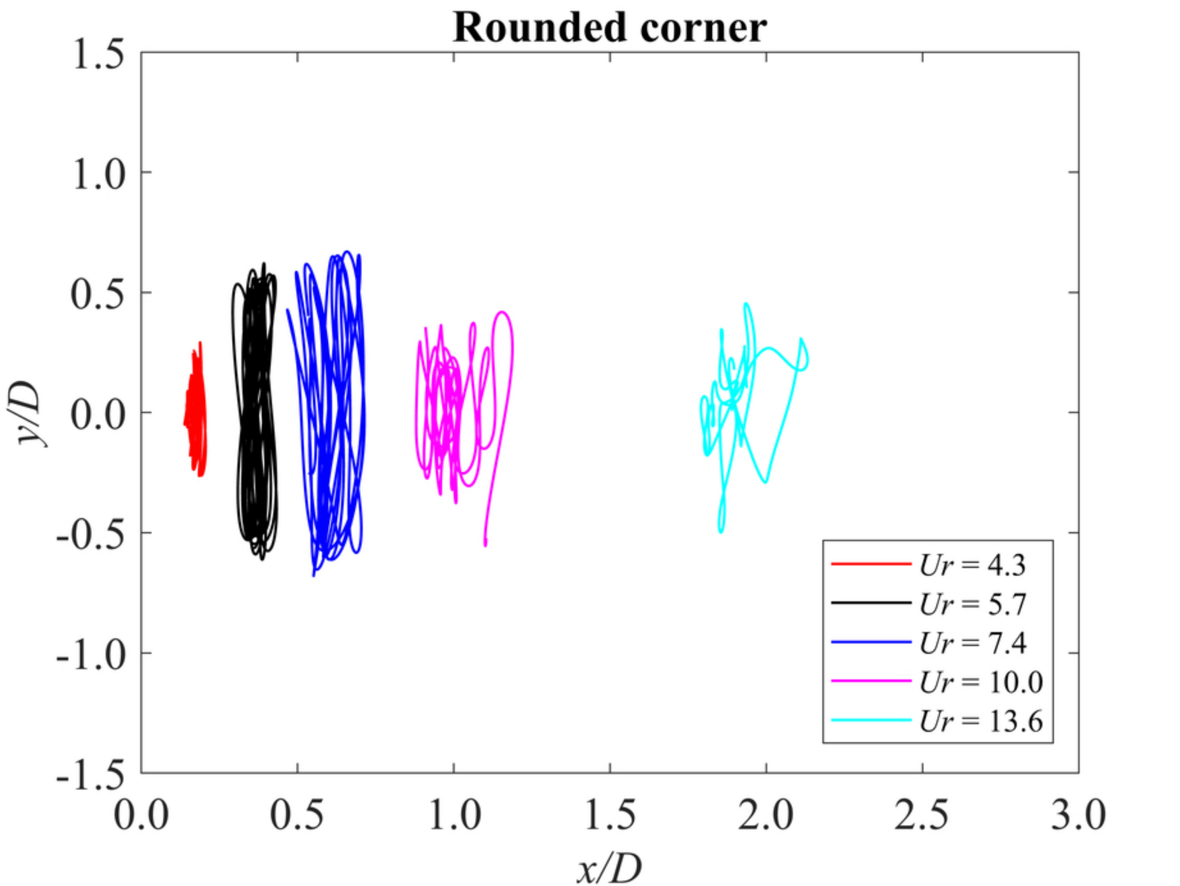

Rounded corner
1.5
1.0
0.5
0.0
-0.5
-1.0
-1.5
y/D
0.0
0.5
1.0
1.5
2.0
2.5
3.0
x/D
Ur = 4.3
Ur = 5.7
Ur = 7.4
Ur = 10.0
Ur = 13.6

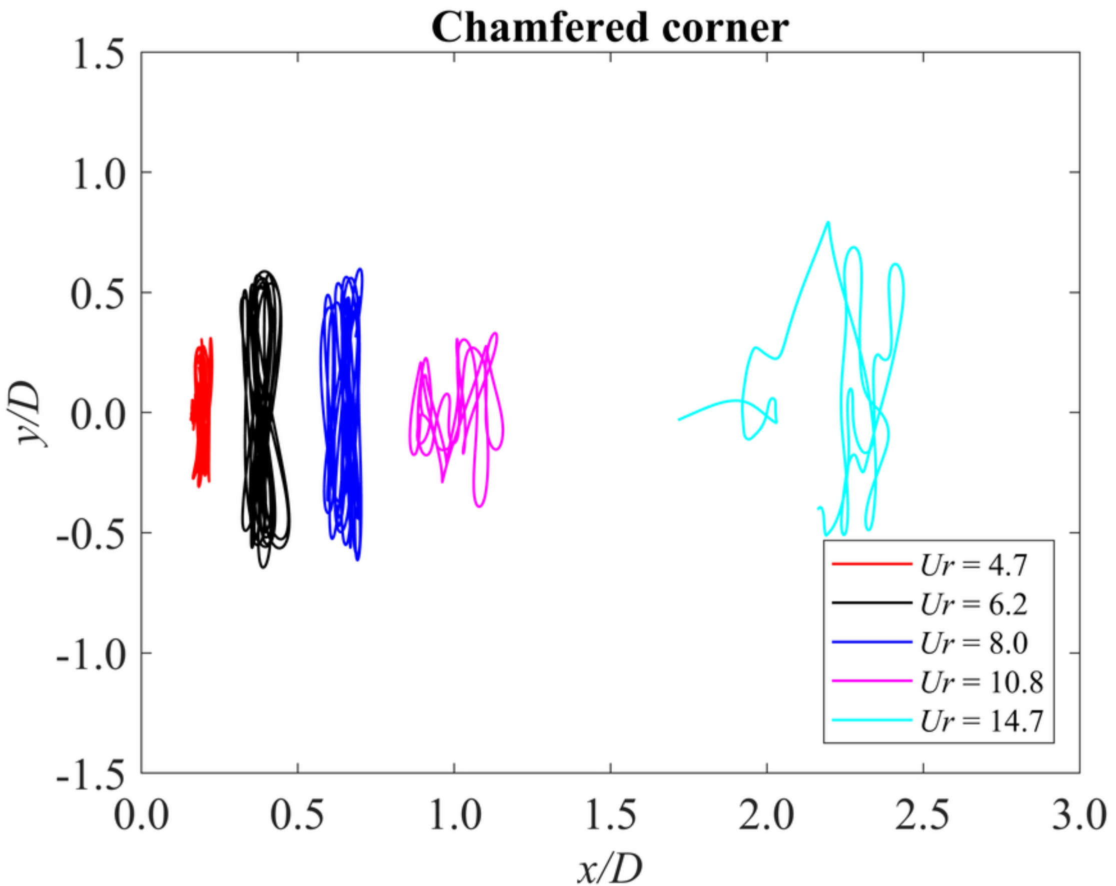

Chamfered corner
1.5
1.0
0.5
0.0
-0.5
-1.0
-1.5
y/D
0.0
0.5
1.0
1.5
2.0
2.5
3.0
x/D
Ur = 4.7
Ur = 6.2
Ur = 8.0
Ur = 10.8
Ur = 14.7

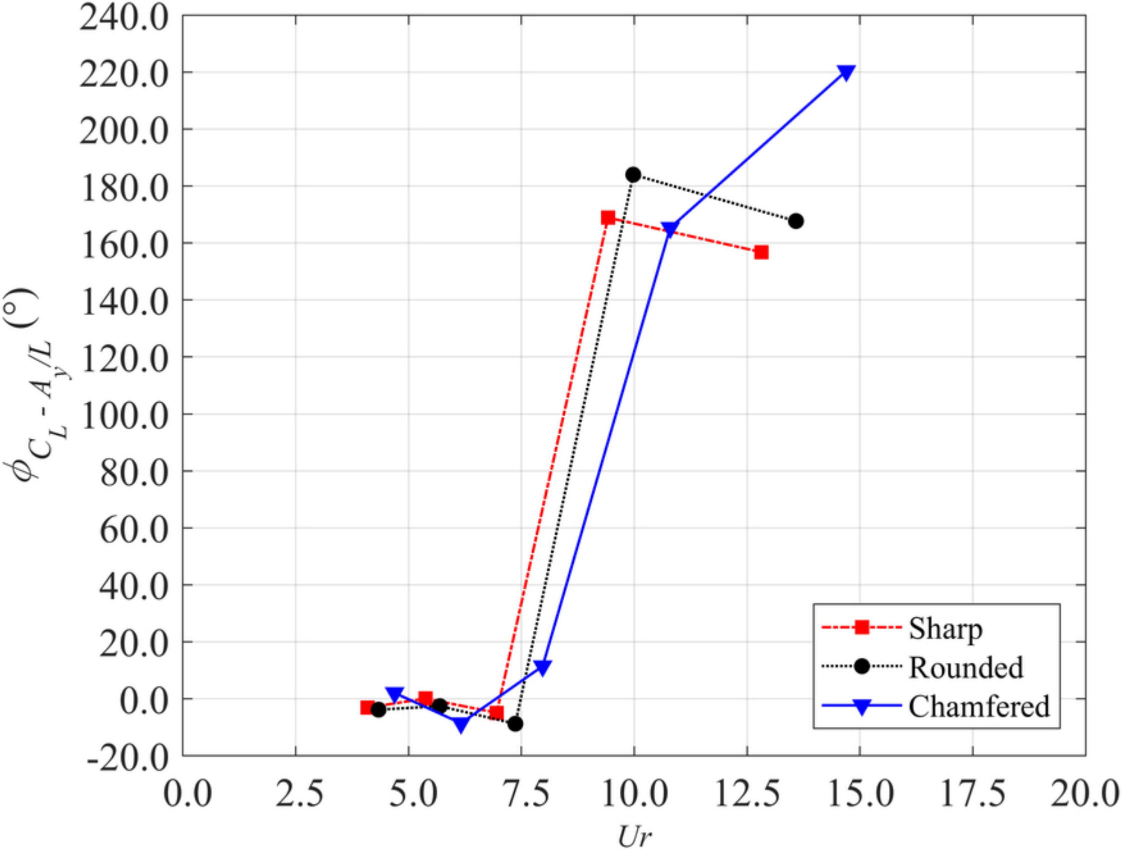

240.0
220.0
200.0
180.0
160.0
140.0
120.0
100.0
80.0
60.0
40.0
20.0
0.0
-20.0
0.0
2.5
5.0
7.5
10.0
12.5
15.0
17.5
20.0
$\phi_{C_L - A_y/L}$ (°)
$Ur$
Sharp
Rounded
Chamfered

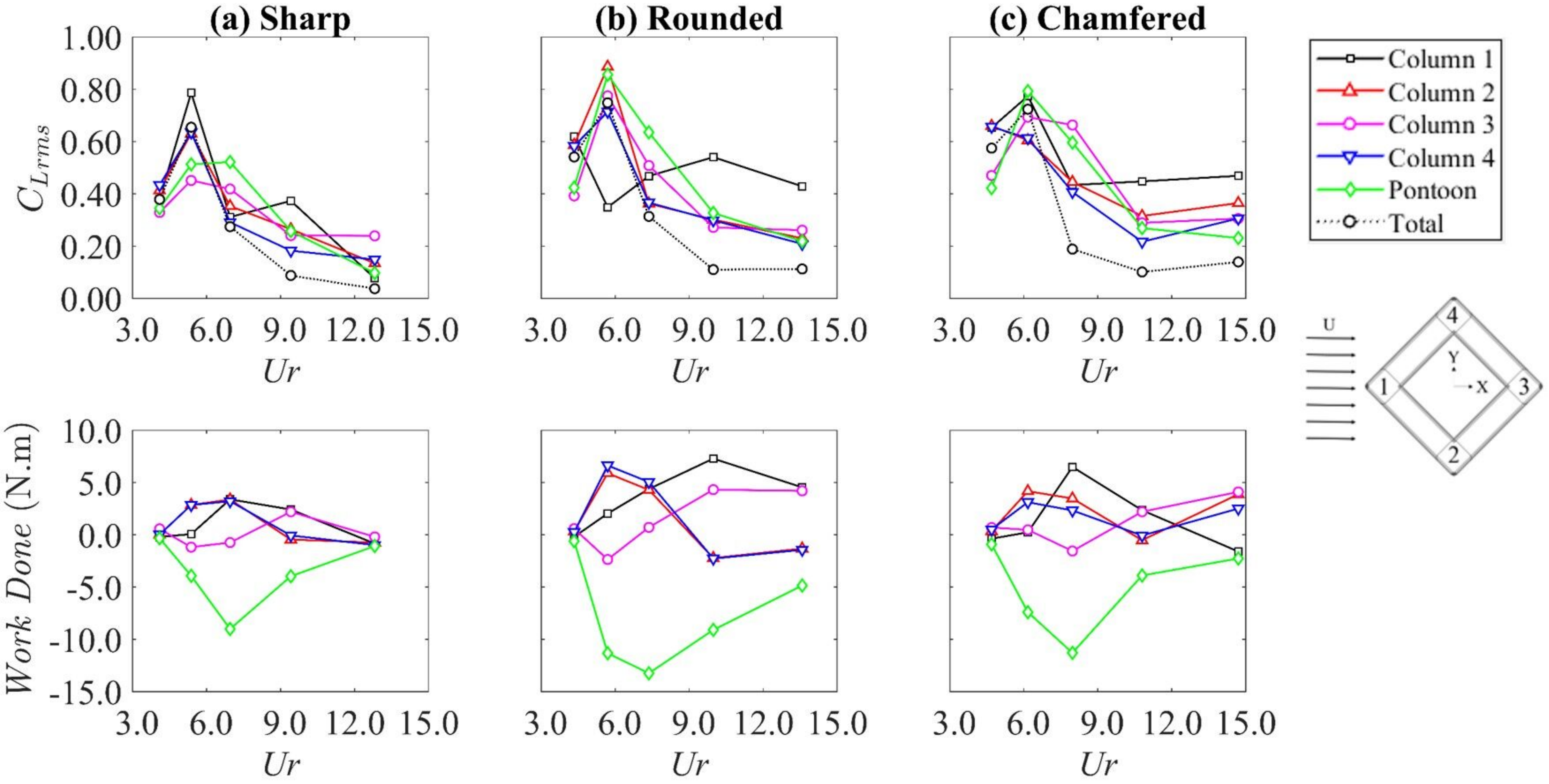

(a) Sharp
(b) Rounded
(c) Chamfered
$C_{Lrms}$
Work Done (N.m)
Ur
Column 1
Column 2
Column 3
Column 4
Pontoon
Total
U
1
2
3
4
X
Y

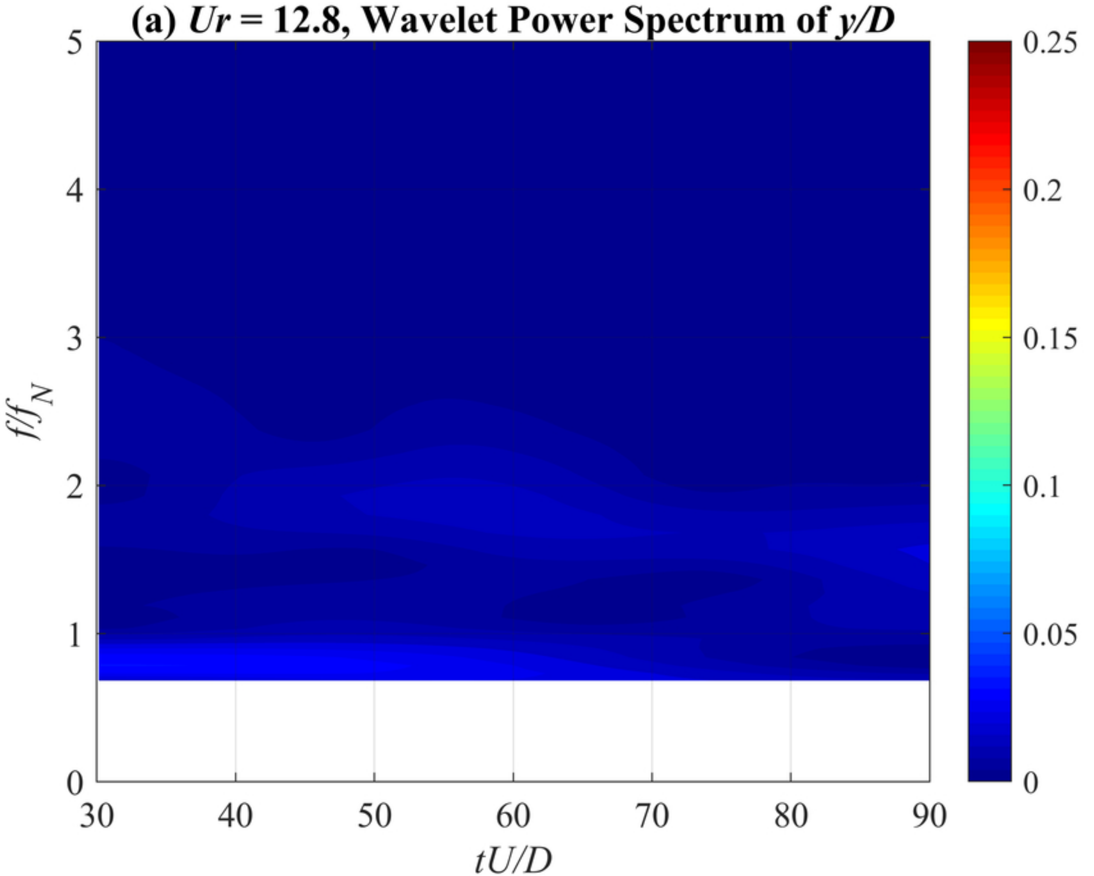
(a) Ur = 12.8, Wavelet Power Spectrum of y/D
f/f_N
0
1
2
3
4
5
30
40
50
60
70
80
90
tU/D
0
0.05
0.1
0.15
0.2
0.25

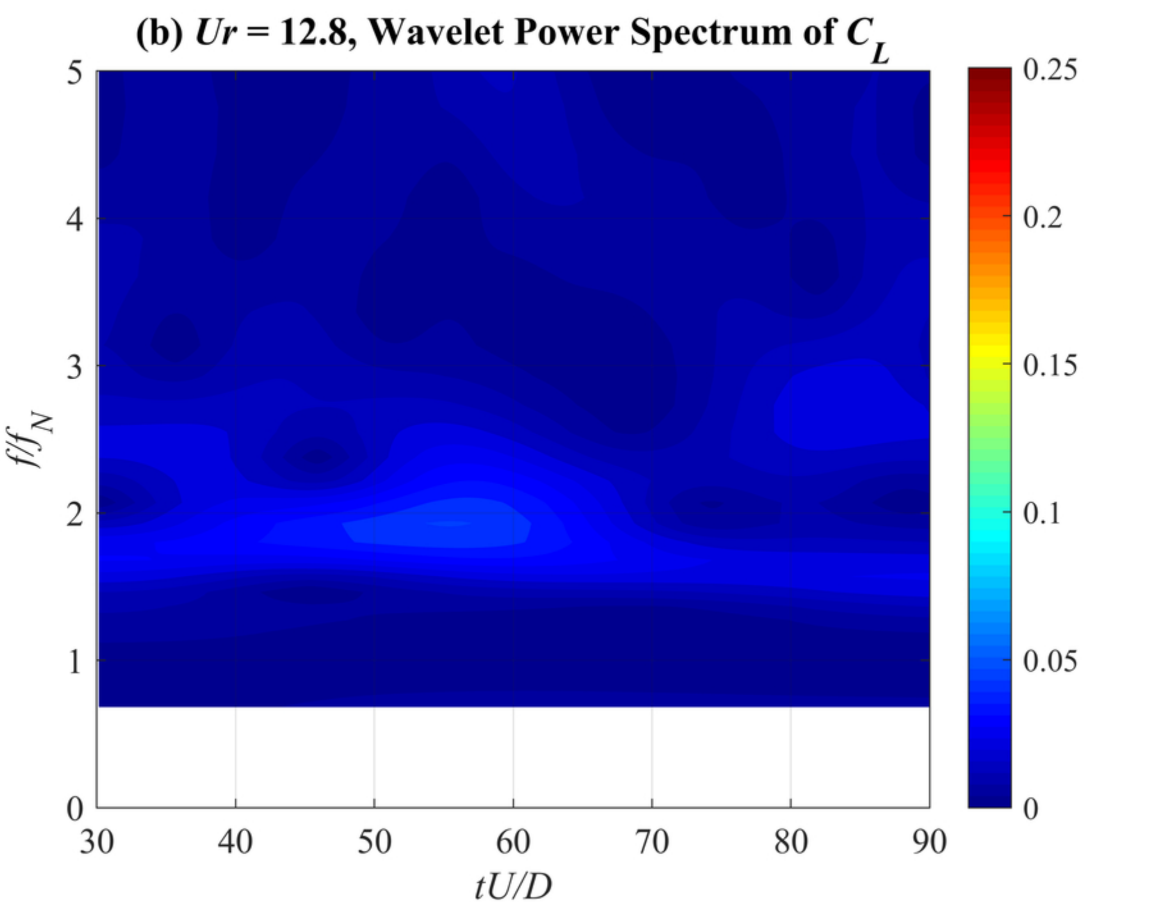

(b) Ur = 12.8, Wavelet Power Spectrum of C_L
f/f_N
tU/D
0
1
2
3
4
5
30
40
50
60
70
80
90
0
0.05
0.1
0.15
0.2
0.25

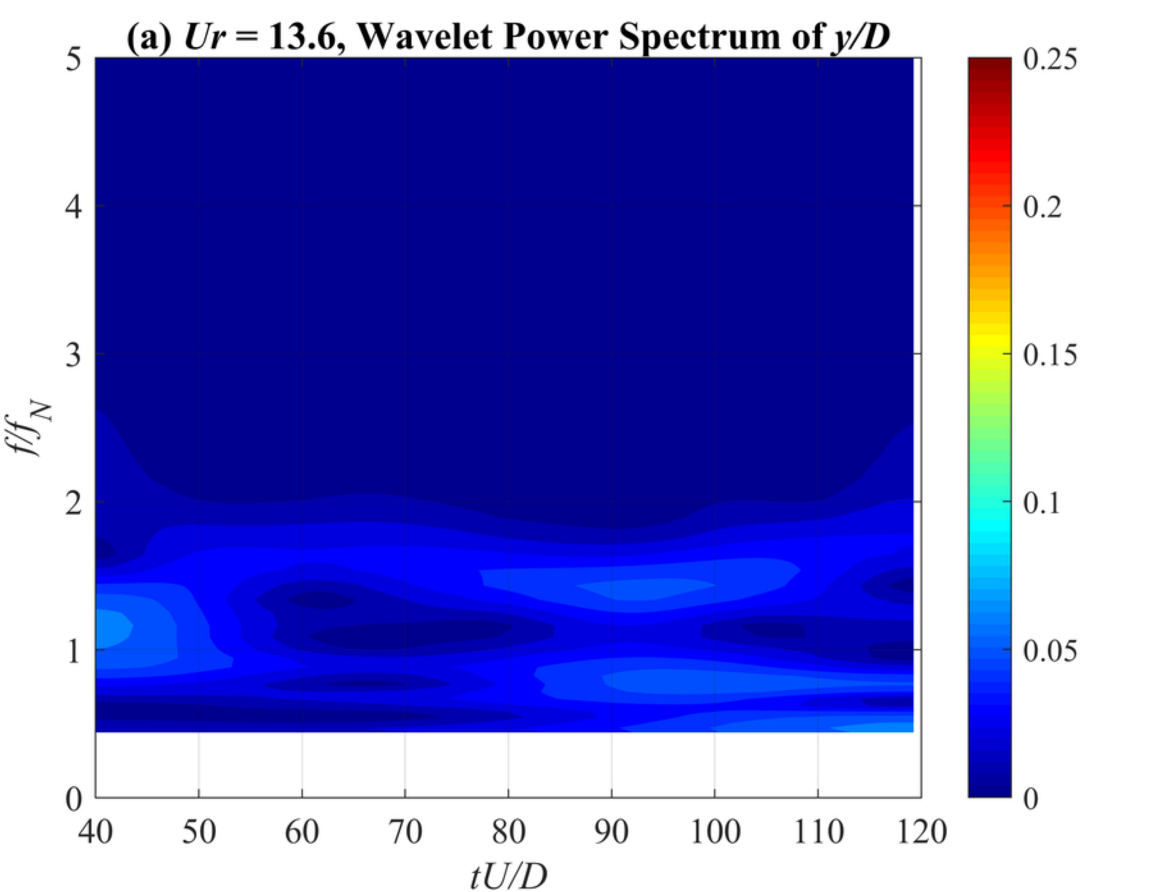

(a) Ur = 13.6, Wavelet Power Spectrum of y/D
f/f_N
tU/D
0
1
2
3
4
5
40
50
60
70
80
90
100
110
120
0
0.05
0.1
0.15
0.2
0.25

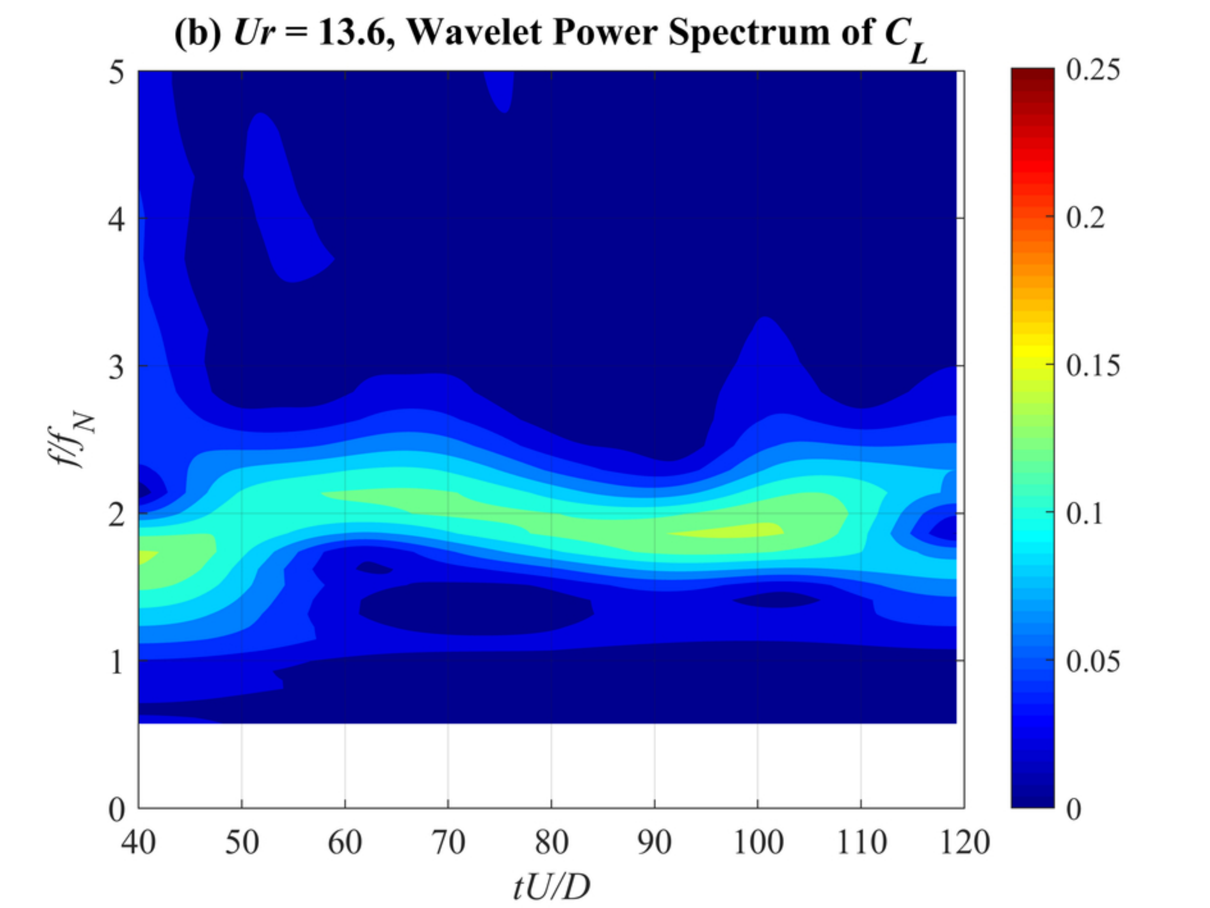

(b) Ur = 13.6, Wavelet Power Spectrum of C_L
f/f_N
tU/D
0
1
2
3
4
5
40
50
60
70
80
90
100
110
120
0
0.05
0.1
0.15
0.2
0.25

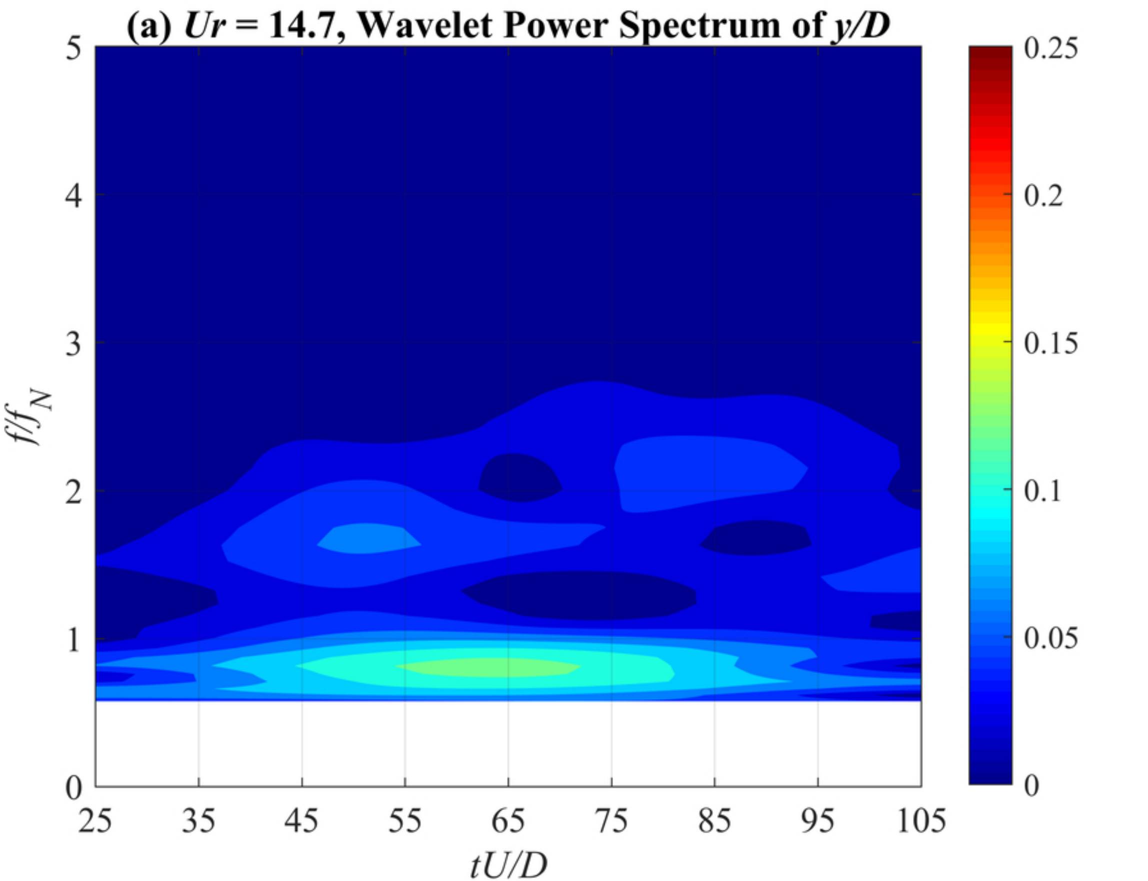

(a) *Ur* = 14.7, Wavelet Power Spectrum of *y/D*
$f/f_N$
0
1
2
3
4
5
25
35
45
55
65
75
85
95
105
$tU/D$
0
0.05
0.1
0.15
0.2
0.25

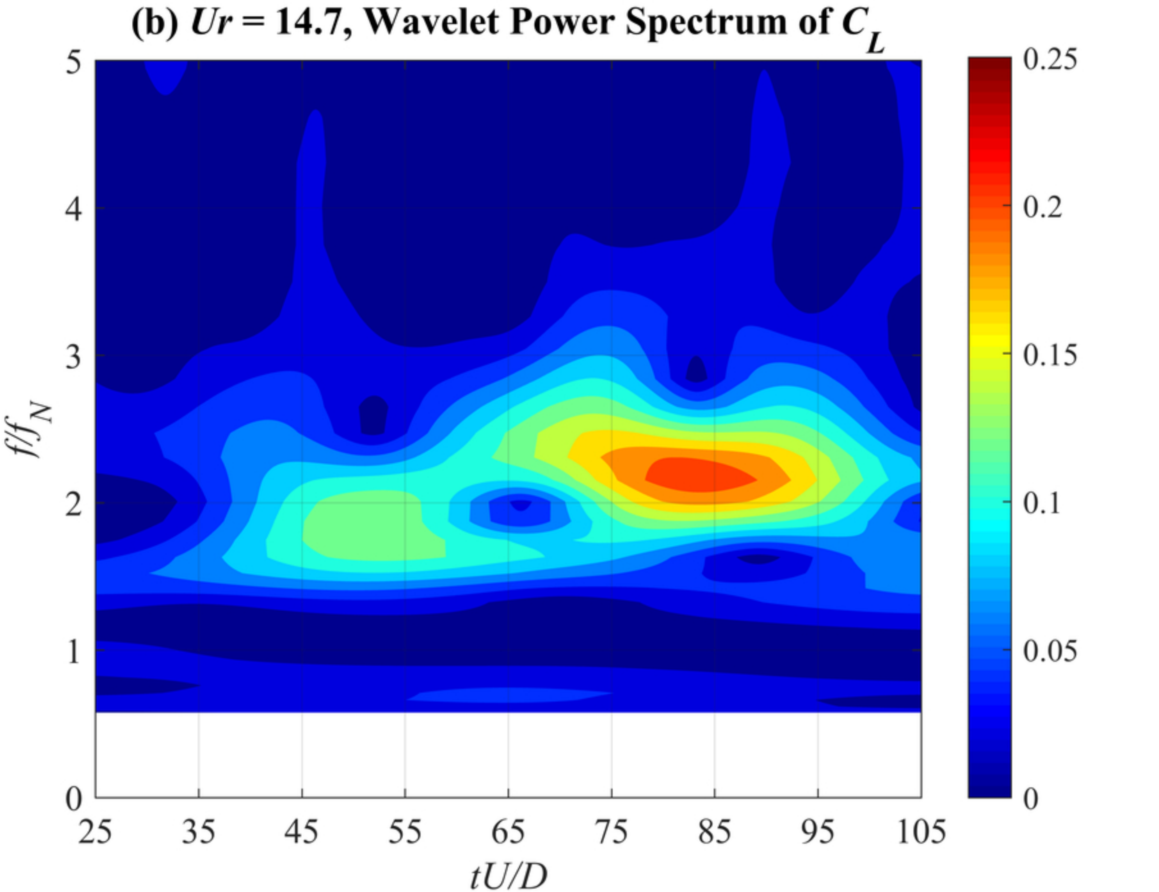
(b) Ur = 14.7, Wavelet Power Spectrum of C_L
f/f_N
tU/D
0
1
2
3
4
5
25
35
45
55
65
75
85
95
105
0
0.05
0.1
0.15
0.2
0.25

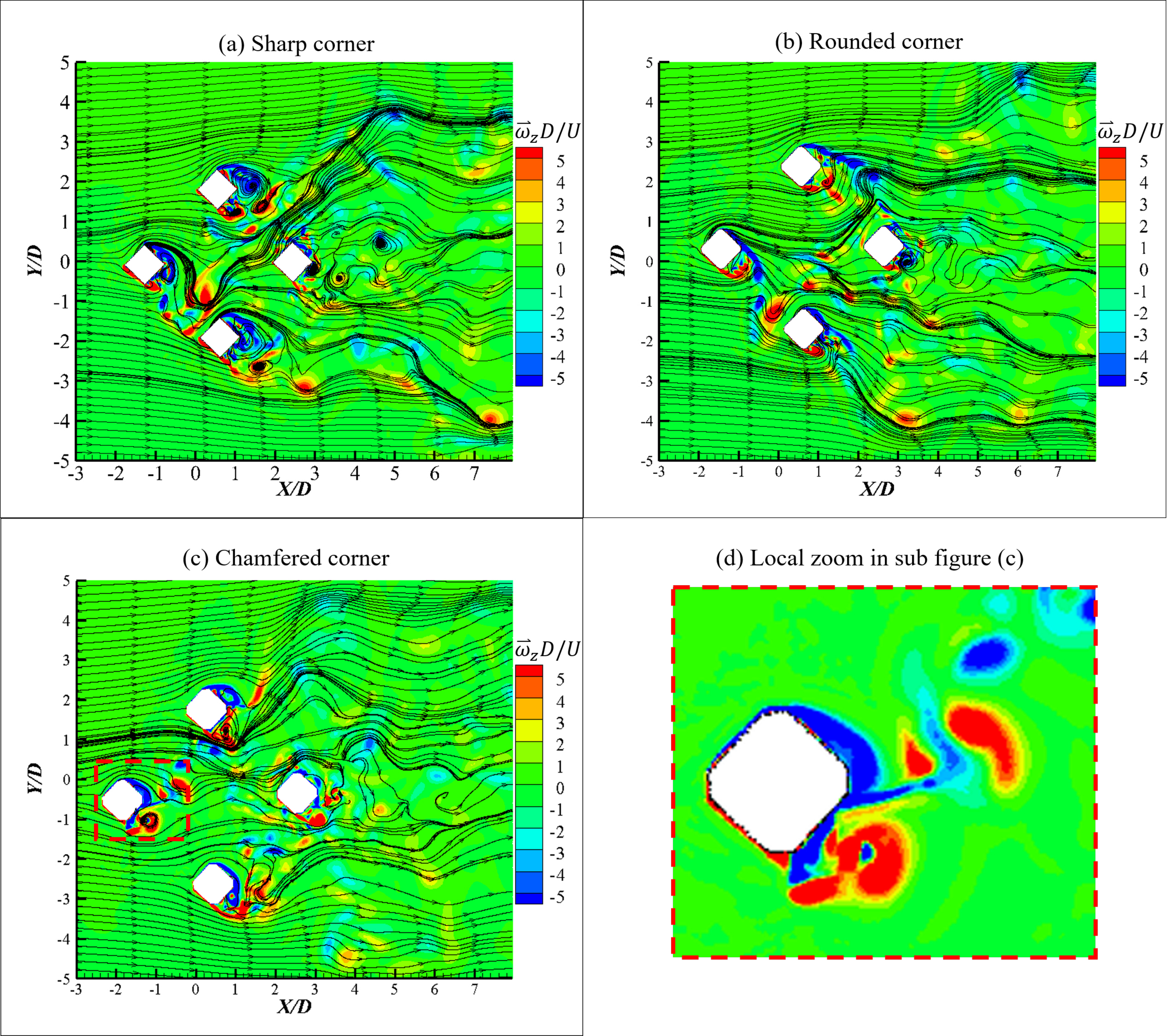

(a) Sharp corner
(b) Rounded corner
(c) Chamfered corner
(d) Local zoom in sub figure (c)
Y/D
X/D
$\vec{\omega}_z D/U$
5
4
3
2
1
0
-1
-2
-3
-4
-5

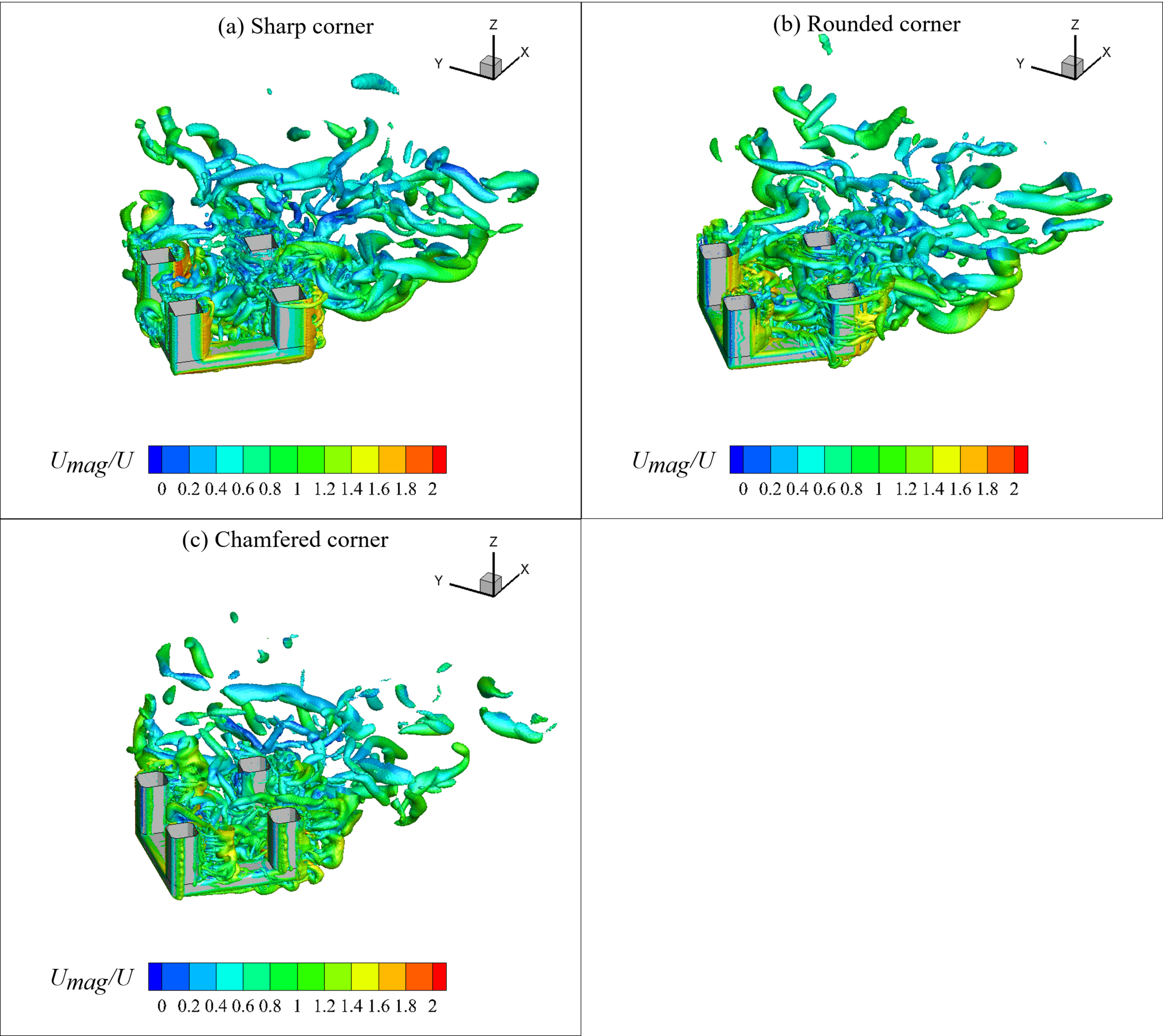
(a) Sharp corner
Z
Y
X
Umag/U
0 0.2 0.4 0.6 0.8 1 1.2 1.4 1.6 1.8 2
(b) Rounded corner
Z
Y
X
Umag/U
0 0.2 0.4 0.6 0.8 1 1.2 1.4 1.6 1.8 2
(c) Chamfered corner
Z
Y
X
Umag/U
0 0.2 0.4 0.6 0.8 1 1.2 1.4 1.6 1.8 2